Summer 7-30-2015

Improving Nocturnal Fire Detection with the VIIRS Day-Night Band

Thomas N. Polivka
University of Nebraska-Lincoln, thomas.polivka@huskers.unl.edu

IMPROVING NOCTURNAL FIRE DETECTION WITH THE VIIRS DAY-NIGHT BAND

by

Thomas N. Polivka

A THESIS

Presented to the Faculty of

The Graduate College at the University of Nebraska

In Partial Fulfilment of Requirements

For the Degree of Master of Science

Major: Earth and Atmospheric Sciences

Under the Supervision of Professor Jun Wang

Lincoln, Nebraska

August, 2015

IMPROVING NOCTURNAL FIRE DETECTION WITH THE VIIRS DAY-NIGHT BAND

Thomas N. Polivka, M.S.

University of Nebraska, 2015

Adviser: Jun Wang

As an important component in the Earth-atmosphere system, wildfires are a serious threat to life and property that—despite improving warning systems—have exacted greater costs in recent years. In addition, they impact global atmospheric chemistry by releasing potent trace gasses and aerosols. Using the Visible Infrared Imaging Radiometer Suite (VIIRS), this study investigates the adjustment of fire pixel selection criteria to include visible light signatures at night, creating the Firelight Detection Algorithm (FILDA). This allows for greatly improved detection of smaller and cooler fires from satellite observations. VIIRS scenes with coincident Advanced Spaceborne Thermal Emission and Reflection (ASTER) overpasses are examined after applying the operational VIIRS fire product algorithm and including a modified candidate fire pixel selection approach, which lowers the 4 μm brightness temperature threshold from 305 K but includes a minimum day-night band (DNB) radiance. FILDA is tested by applying it to scenes in different environments, including large forest fires like the Rim Fire in California and High Park fire in Colorado, in addition to gas flares. A large increase in the number of detected fire pixels is observed with small non-agricultural wildfires, as verified with the finer-resolution ASTER data (90 m). Quantitative use of the DNB to improve detection of these smaller fires could lead to reduced warning and response times as well as provide more accurate quantification of biomass burning emissions at night.

DEDICATION

This work is dedicated to my family and friends who have always supported me in everything I strive to achieve. Without them, this work would not have been possible.

ACKNOWLEDGMENTS

Foremost, my advisor, Dr. Jun Wang, deserves special thanks for constructing an environment that promotes learning, excellence, and camaraderie within his research group. He motivated me to better myself, improve my skills, and persevere. Dr. Edward Hyer also deserves special thanks for two summers I interned at the Naval Research Laboratory in Monterey, CA under his supervision. He, as well as Dr. Dave Peterson, proved to be fantastic mentors.

During graduate school, I was fortunate to be selected as the System Administrator for the department, at the behest of Dr. Clinton Rowe and Dr. Adam Houston. They were patient as I learned the ins-and-outs of Linux administration. I thank Dr. Clinton Rowe and Dr. Steve Hu for their insight and ideas to improve my thesis as my committee members.

I also acknowledge Luke Ellison for his programming abilities and help with correcting pixel overlap. In addition, while working on my undergraduate degree, I thank Dr. David Changnon for being my advisor, whose enthusiasm for teaching encouraged me to attend graduate school.

Contents

List of Figures

List of Tables

Chapter 1

Introduction

As an important component in the Earth-atmosphere system, wildfires are a serious threat to life and property that—despite improving warning systems (Westerling et al., 2006; Haynes et al., 2010)—have exacted greater costs in recent years. In addition, they impact global atmospheric chemistry by releasing potent trace gasses such as carbon monoxide, carbon dioxide, methane, and ethene (Hao et al., 1996), as well as aerosols and black carbon (Ichoku and Kaufman, 2005). These by-products of combustion are capable of travelling large distances and impacting health and meteorological processes in remote locations (Wang et al., 2006; Duck et al., 2007), and in addition to creating local pollution hazards, can affect Earth's climate (van der Werf et al., 2010). Fire-spawned smoke aerosols have complex interactions with the atmosphere by causing a reduction in surface illumination and radiative forcing (Kaufman et al., 1997; 2002), while simultaneously warming the atmosphere, which decreases vertical temperature gradients and increases atmospheric stability (Ramanathan et al., 2001) due to their relatively low single-scattering albedo (Dubovik et al., 1998). As a consequence of wildfire lethality and potential for property damage, earlier detection of wildfires via remote sensing is paramount to proper allocation of fire-management resources (Flasse et al., 2004; Davies et al., 2009). These effects stress the importance of accurately

detecting and characterizing fires as well as accurately quantifying global emissions from biomass burning.

The launch of the Suomi National Polar-orbiting Partnership (S-NPP) satellite on 28 October 2011 has opened up unprecedented capabilities with the Visible Infrared Imaging Radiometer Suite (VIIRS). With a heritage extending back over 40 years to the Defense Meteorological Satellite Program (DMSP) *S*ensor *A*erospace Vehicle Electronics *P*ackage (SAP), first launched in 1970, the Advanced Very High Resolution Radiometer (AVHRR) (1978), and the MODerate Resolution Imaging Spectroradiometer (MODIS) (1999), VIIRS boasts improved spatial resolution and a higher signal-to-noise ratio than previous sensors. VIIRS has already shown promise in detecting smaller and cooler fires (Schroeder et al., 2014) than what MODIS currently is capable of. This paper presents a novel approach to detecting small fires by employing the day-night band (DNB) aboard VIIRS, which detects visible and near-infrared (NIR) emissions at night.

This paper is divided into five chapters, as follows: in Chapter 2, we present a brief history of NASA/NOAA-based fire detection from first observations to today. In Chapter 3, the characteristics of VIIRS and its data are described in detail. The Advanced Spaceborne Thermal Emission and Reflection (ASTER) sensor, used for validation, is also described in that chapter. Afterwards, we discuss the methods employed to improve the detection of smaller and cooler fires in Chapter 4. We then discuss the results and validation in Chapter 5, and in Chapter 6, we finish with a discussion of our findings and main conclusions.

Chapter 2

Pre-VIIRS NASA/NOAA Satellite-Based Fire Detection

Weather satellites have played a pivotal part in the understanding of the Earth-atmosphere system since 1 April 1960, when NASA launched the first weather satellite, the Television Infrared Observation Satellite (TIROS-1), into orbit. TIROS-1 carried a television camera that only pointed at the Earth for short portions of its orbit (over North America). Convinced by TIROS-1's success in monitoring meteorological conditions, the Air Force launched its own classified military satellite program in 1962, the Defense Meteorological Satellite Program (DMSP). Subsequent satellite launches (organized into "Blocks" based on satellite generation) improved upon sensor and bus design. In order to monitor nocturnal cloudcover, the DMSP Blocks 5A, B, and C (1970-1975) were capable of observing low-light environments at night with the *S*ensor *A*erospace Vehicle Electronics *P*ackage (SAP) (Elvidge et al., 1999). The SAP carried two sensors, one for visible and the other for infrared radiation. The visible sensor was capable of observing nocturnal scenes, as the spectral response was quite broad: the half power response points were at 0.57 μm and 0.97 μm with the peak at around 0.8 μm (Dickinson et al., 1974). Data from the nocturnal scenes had a resolution of approximately

3.7 km near sub-satellite point. Using the SAP's visible channel, Croft (1973) was the first person to qualitatively demonstrate its potential for monitoring gas flaring, savannah brush fires, and cooking fires over Africa during the night. In 1976, DMSP Block 5D was launched, and carried a new instrument that improved upon the SAP's design: the Operational Line-scan System (OLS). Like the SAP, the OLS has a very broad band covering the visible and NIR portion of the spectrum with a "smoothed" spatial resolution of approximately 2.7 km. The instrument was also noted by Croft (1978) to be excellent at qualitatively observing gas flares as well as city lights (Welch, 1980). The DMSP data were eventually declassified and made available to scientists, who used the sensor to globally map cities and human settlements based on their light emission (Elvidge et al., 1997; 1999).

Unrelated to the DMSP, subsequent NASA TIROS satellites improved upon the original satellite design, and following collaboration with NOAA, the TIROS-N satellite launched in 1978. TIROS-N brought digital data transmission, rather than analog as in previous NASA satellites (Hastings and Emery, 1992). In addition, TIROS-N carried a powerful instrument for its time: the Advanced Very High Resolution Radiometer (AVHRR). AVHRR/1 was a scanning radiometer which sensed the Earth in four channels (increased to five on later AVHRR sensors). The four channels spanned several different sectors of the electromagnetic spectrum with a resolution of 1.09 km at nadir (Hastings and Emery, 1992): channel 1 sensed a portion of the visible spectrum (0.58 - 0.68 μm); channel 2 recorded the near-infrared (0.725 - 1.00 μm); channel 3, being a hybrid channel, utilized two different IR signatures of 1.58 - 1.64 μm (channel 3a, shortwave infrared) and 3.55 - 3.93 μm (channel 3b, mediumwave infrared); and lastly, channel 4 covering 10.30 - 11.30 μm. A thorough description of the AVHRR sensor and its orbital characteristics can be seen in Table 2.1; channel 5 was added with AVHRR/2. The AVHRR datastream has continued uninterrupted since its launch in 1978, giving a remarkable history of the how the Earth's surface and atmosphere has changed through the decades.

Using AVHRR's channels 3b (centered at 3.74 μm) and 4 (centered at 10.8 μm), Dozier (1981) developed a bi-spectral approach to identify hot sources and quantitatively estimate the area occupied by the hot target in an unsaturated pixel. Channel 3b, spanning 3.55 to 3.93 μm, was noted to be sensitive to hot sources such as steel mills in the Ohio and gas flares in the Middle East (Matson and Dozier, 1981), which can be explained by the Planck function:

$$B_\lambda(T) = \frac{2hc^2}{\lambda^5 e^{\frac{hc}{k_B \lambda T}} - 1} \tag{2.1}$$

where $B_\lambda(T)$ is the radiance emitted at a specific wavelength, T is the temperature in kelvins, c is the speed of light in a vacuum ($c = 2.998 \times 10^8$ m·s^{-1}), h is Planck's constant ($h = 6.626 \times 10^{-34}$ J·s), and k_B is the Boltzmann's constant ($k_B = 1.381 \times 10^{-23}$ J·K^{-1}). Flaming wildfires typically have kinetic temperatures between 800 K and 1200 K (sometimes as hot as 1800 K) and smoldering temperatures between 450 K and 800 K (Lobert and Warnatz, 1993); at a temperature of 1000 K, the peak radiance is around 2.9 μm. As

Table 2.1: Spacecraft and channel information for the NOAA-19 AVHRR

Orbital altitude:	870 km
Inclination:	98.7°
Orbital period:	102.14 min.
Ascending equator local crossing time:	13:39:39
Image Width:	2048 pixels
Swath width:	∼2800 km
IFOV:	∼1.4 μradians
Spatial resolution:	∼4 km

Channel	Description	Spectral Range (μm)
1	Visible green channel	0.58 - 0.68
2	Reflected IR channel	0.73 - 1.00
3A	Reflected IR channel	1.58 - 1.64
3B	Reflected IR/Thermal IR channel	3.55 - 3.93
4	Thermal IR channel	10.30 - 11.30
5	Thermal IR channel	11.50 - 12.50

smoldering ground (T = 600 K) has peak emission at 4.8 μm, the combination of the two combustion types lies very close to the spectrum of channel 3b (3.55 - 3.93 μm). However, by the same logic, the influence of the fires in channel 4 (10.3 - 11.3 μm) are minimal in comparison, which is why it is used to contrast against the ∼4 μm channel. In addition to the signal difference between the two channels, the approach also depended on an accurate assumption of a background temperature—the surface kinetic temperature of the portion of the pixel that was not occupied by the heat source. This was assumed to be represented by the ∼4 μm brightness temperature (BT) of a similar adjacent pixel (Matson and Dozier, 1981). It should be noted, however, that Giglio and Kendall (2001) later showed that averaging neighboring pixel BTs for 4 and 11 μm could be used instead of estimating the surface background kinetic temperature. Using the approach in Dozier (1981), Matson and Dozier (1981) performed the first estimation of gas flare and steel mill temperatures and areas using AVHRR's infrared bands, as AVHRR was not capable of detecting visible light at night—this was the first time fires were observed from satellite via the infrared bands alone. Several scientists (including Flannigan and Vonderhaar, 1986; Robinson, 1991) used this relationship to investigate the global distribution and frequency of wildfires. Today, fire detection algorithms have evolved from AVHRR into the realm of other sensors, and at their heart, they are still based on that principal: the difference in radiance/brightness temperature (BT) between 4 μm and 11 μm (Prins et al., 1998; Prins and Menzel, 1992; Justice et al., 2002; Giglio et al., 2003; Csiszar et al., 2013; Peterson et al., 2013; Schroeder et al., 2014).

Several early fire detection algorithms developed for AVHRR identified potential fire pixels according to pre-defined thresholds (e.g. Flasse and Ceccato, 1996; Arino and Melinotte, 1998; Justice et al., 1996). These consisted of the minimum 3.8 μm BT (abbreviated as BT_4) and a minimum difference between 3.8 μm and 10.8 μm BT (abbreviated $BT_4 - BT_{11}$) that a pixel must exceed. For example, in Flasse and Ceccato (1996), any pixel with a BT_4 greater

than 311 K and $BT_4 - BT_{11}$ greater than 8 K was flagged as a potential fire. Only then would additional contextual tests be run, which compared the potential fire pixel to its surrounding pixels. These thresholds were usually tailored to the specific region to be monitored (such as sub-tropical Africa as in Arino and Melinotte, 1998) and had difficulty monitoring fires in radically different environments (Li et al., 2001). Other algorithms, such as those of Flasse and Ceccato (1996); Justice et al. (1996); Giglio and Kendall (1999), employed contextual tests as well to attempt to further screen out false positives while permitting use of a lower BT_4 threshold. Common to all these algorithms is that they used BT_4 and $BT_4 - BT_{11}$ thresholds that were obtained empirically and somewhat arbitrarily.

Despite AVHRR's power and utility for remotely sensing wildfires globally, it was still largely limited by the large pixel sizes and the fact that fires only occupy a small portion of a full pixel (termed fire fraction). The BT for a pixel consists of the total radiance over the entire pixel area detected by the sensor, which in AVHRR's case, is 1.09 km $\times$ 1.09 km near the sub-satellite point (Hastings and Emery, 1992). This means most fire signals, despite having their peak emission wavelength close to channel 3b's spectral range, are largely drowned out by the background (non-burning) portion of a pixel. AVHRR's 3b and 4 channels also suffer from low saturation temperatures, which depending on the platform and calibration coefficients, varies between 322 and 331 K (Robinson, 1991). In cases of extremely hot fires/targets, the bi-spectral approach from Dozier (1981) readily breaks down (Matson and Holben, 1987). In addition, AVHRR only affords one view per day—and sometimes every two days—across much of the globe. Future instruments would prove to partially overcome these limitations.

Geostationary sensors were in a prime position to supplement the poor temporal resolution of AVHRR, despite their decreased spatial resolution. Beginning in 1980 with the launch of GOES-4, NOAA's GOES systems were equipped with an atmospheric sounder—the Visible and Infrared Spin Scan Radiometer Atmospheric Sounder (VAS). The sensor provided

several bands centered near 4 and 11 μm, allowing for the use of the Dozier (1981) approach, despite a significant caveat: the spatial resolution of the VAS was ∼7 (14) km for 4 (11) μm (Prins and Menzel, 1992), versus AVHRR's ∼1 km. However, the large pixel sizes also meant that the sensor did not saturate nearly as frequently as AVHRR. Prins and Menzel (1992) developed an algorithm that utilized the VAS to identify biomass burning in South America. Unlike the algorithms that used pre-determined BTs as in AVHRR, fire pixels were identified only when BT_4 was 4 K greater than the background BT_4 (termed BT_{4b}) and the BT_{11} was 1 K greater than the background BT_{11} (termed BT_{11b}). Prins and Menzel (1992) proved that the VAS had immense potential in monitoring biomass fires in South America, and although showing promising results, the technique was too cumbersome to perform on an operational level. At the time, the approach required manual smoke and atmospheric correction to account for differences in atmospheric transmittance caused by the water vapor contained in the smoke. Prins and Menzel (1994) released the automated-biomass-burning-algorithm (ABBA), an updated version of the algorithm developed in 1992, but done on a much larger and automated scale. As before, fire pixels were identified after being compared against the background BTs. Background BTs were 11 μm non-fire BTs calculated from 150 km×150 km subsections of the study area after correcting for transmissivity and emissivity. To be classified as fire pixels in the updated algorithm, pixels needed to pass two primary tests: (1) $BT_4 - BT_{11}$ needed to be greater than $BT_{4b} - BT_{11b}$, and (2) $BT_4 - BT_{4b}$ needed to be greater than 2 K or 1.5 times the BT_{4b} standard deviation. This process disqualified 90% of the non-fire pixels (Prins and Menzel, 1994), and afterwards, additional tests were run that accounted for atmospheric transmittance, as the VAS bands showed a moderate degree of water vapor contamination. ABBA was later renamed as Wildfire-ABBA (or WF-ABBA), and has been continually updated and widely used to monitor wildfires and estimate smoke emissions (Reid et al., 2009; Wang et al., 2006), in addition to extending well beyond its GOES heritage to European and Japanese geostationary sensors.

One of the most important fire-detecting spaceborne sensors to date, the *MOD*erate-resolution *I*maging *S*pectroradiometer (MODIS), was launched in 1999. MODIS is a 36 channel instrument, which covers a spectrum from 0.4 to 14.4 µm, with spatial resolutions of 250 m (bands 1-2), 500 m (bands 3-7), and 1 km (bands 8-36). A second MODIS instrument was launched in 2002, and as it is carried the on two separate satellite platforms Terra and Aqua, provides two to four daylight scenes of the continental United States each day (and two to four more at night). While MODIS was designed for a wide variety of scientific applications, its 3.9 and 11 µm channels were specifically designed for fire detection with saturation temperatures of 450 and 400 K, respectively (Kaufman et al., 1998b). The MODIS fire detection algorithm, like the AVHRR algorithms before it, is based on the idea that the BT_4 band will be more sensitive to fires than the BT_{11} band (Justice et al., 2002). It has undergone numerous revisions over the years, and the latest publicly available version—MODIS Collection 5—still relies on pre-specified thresholds. The original MODIS fire detection algorithm consisted of a combination of absolute and relative tests (Kaufman et al., 1998a; Justice et al., 2002) and was designed to minimize false positives. Giglio et al. (2003) updated the MODIS algorithm and greatly enhanced its performance with detection of smaller and cooler fires. The primary mechanisms of improvement were lowering the thermal thresholds and including contextual tests, which compared potential fire pixels to their surroundings.

MODIS ushered in an unparalleled level of satellite-based fire research—not only in terms of fire detection—but fire characterization as well. Kaufman et al. (1998a;b), for example, developed the concept of fire radiative power (FRP). FRP, which is a quantitative measure of fire intensity based solely on a ∼4 µm channel (Kaufman et al., 1998b; Ichoku et al., 2008; Peterson et al., 2013), was shown to be correlated with smoke emissions (Ichoku and Kaufman, 2005; Peterson and Wang, 2013). In addition, the MODIS fire products were also greatly improved upon when compared to AVHRR and other sensors. For example,

identifying the utility of satellite-based fire detection for fire suppression resource allocation, the U.S. Forest Service requested quicker availability of the MODIS fire products. The MODIS Rapid Response fire product was created as a result, which disseminated fire data within hours of MODIS data acquisition (Justice et al., 2002). Until that point, satellite data was useful for fire monitoring, but not for detection and response.

While fires were first seen and thought to be detectable by satellite with visible data observed at night (Croft, 1973), quantitative characterization and detection of fire activity from space over the last 40 years has mainly relied on satellite-measured infrared data. Here, we take advantage of the DNB's high spatial resolution of 0.74×0.74 km and radiometric calibration aboard VIIRS and continue pursuing the ideas that Croft proposed over 40 years ago: combining both visible and infrared data to detect fires, creating the *FI*re*L*ight *D*etection *A*lgorithm (FILDA). Furthermore, we evaluate our approach using ASTER's 90 meter infrared data.

Chapter 3

Instruments and Data

3.1 VIIRS

The most recent Earth-observing radiometer, VIIRS, was launched on 28 October 2011, and will eventually replace MODIS for operational fire detection. Located aboard Suomi National Polar-orbiting Partnership (S-NPP), VIIRS is a 22-band scanning radiometer with a nominal spatial resolution of 375 m in the five imagery bands (I-bands) and 750 m in both the 16 moderate resolution bands (M-bands) and the DNB (Cao et al., 2014; Wolfe et al., 2013; Schroeder et al., 2014; Csiszar et al., 2013). The sensor data records (SDR) of calibrated radiances and BTs cover a spectral range from 0.411 μm to 11.87 μm and are used in a wide range of Earth observation applications including fire detection and characterization, retrieval of cloud and aerosol properties, and land and sea surface temperature estimation (Hillger et al., 2013). The VIIRS sensor was designed to improve upon legacy instruments, such as MODIS, AVHRR, and the OLS. One significant enhancement relative to these legacy sensors is that VIIRS does not experience the significant off-nadir pixel growth affecting sensors like MODIS, despite its substantially larger swath width; VIIRS pixels at the scan edge are only four times the size of nadir pixels, while MODIS exhibits a growth factor

of nearly ten, for example (Wolfe et al., 2013). For the M-bands, VIIRS delivers SDRs of calibrated radiances and brightness temperatures with an instantaneous field of view (IFOV) of 0.74 × 0.78 km at nadir, which increases to 1.60 × 1.58 km at the edge of the scan (Cao et al., 2014), while the five imagery bands have smaller IFOVs ranging from 0.37 × 0.39 km to 0.80 × 0.79 km at the scan edge. General VIIRS and S-NPP characteristics can be seen in Table 3.1.

Like the OLS, in order to reduce off-nadir pixel growth, VIIRS aggregates samples depending on the sensor scan angle. This is accomplished by employing asymmetrical detectors in conjunction with a unique sample aggregation scheme, which combines multiple samples from one rectangular detector into single raw data record (RDR) pixels consisting of digital counts (see Figure A.1 for an illustration). This processing is done onboard the satellite, except for the dual-gain bands (M1-5, 7, and 13) whose aggregation is done on the ground (Wolfe et al., 2013). As a result, the RDR has three aggregation zones. The 3:1 aggregation zone refers to scan angles between 0° (nadir) and 31.72°, where the value of each

Table 3.1: General Suomi-NPP and VIIRS sensor characteristics (Liao et al., 2013; Wolfe et al., 2013; Cao et al., 2014).

Launch date:	28 October 2011
Orbit description:	Near-circular, near-polar, sun-synchronous
Mean orbital altitude:	840 km
Inclination:	98.7°
Orbital period:	101.5 min.
Ascending equator local crossing time:	13:30 ± 10 min.
Image Width (pixels):	6400 (I-bands), 3200 (M-bands), 4064 (DNB)
Swath width:	≈3000 km
Number of bands	5 I-bands, 16 M-bands, 1 DNB
Nominal spatial resolution	375 m (I-bands), 750 m (M-bands, DNB)
Spectral range	0.411–11.87 μm
Detectors per band	32 (I-bands), 16 (M-bands), 672 (DNB)
Lines per scan	32 (I-bands), 16 (M-bands, DNB)

pixel is actually the average of three individual samples. Similarly, in the 2:1 aggregation zone (scanning angles between 31.72° and 44.86°), two samples from the same detector are aggregated to form a pixel. No sample aggregation is performed in the 1:1 aggregation zone (scan angles greater than 44.86°); thus, each pixel is calculated from a single detector sample. Once the RDR has been generated, it is later processed into a calibrated SDR, retaining the characteristics from aggregation (Polivka et al., 2015).

Unlike MODIS, VIIRS is able to detect visible light and NIR radiation at night with the DNB. The band has a broad spectral response (0.5−0.9 μm) that is sensitive to city lights, volcanoes, lunar illumination, and wildfires, in addition to phenomena such as aurora, bioluminescence, and airglow, for example (Miller et al., 2005; Lee et al., 2006; Miller et al., 2012; Liao et al., 2013). In order to capture the wide range of radiances reflected and emitted from the Earth's surface, the DNB employs three modes of operation: a low-gain, medium-gain, and a high-gain stage (the latter of which contains two redundant focal plane arrays to eliminate noise). The low-gain stage is used for sunlit areas, the medium-gain stage is used for twilight areas, while the high-gain is used for nocturnal scenes. These gains are automatically determined by the onboard electronics module, which can switch

Table 3.2: Nighttime band information for VIIRS (Liao et al., 2013; Cao et al., 2014). Bands in bold font are used for fire detection.

Band	Spectral Range (μm)	Central λ (μm)	Specification Maximum[1]	Gain
M7	0.843 - 0.881	0.86	349	Single
M8	1.225 - 1.252	1.24	165	Single
M10	1.571 - 1.629	1.60	71.2	Single
M12	3.598 - 3.791	3.69	353	Single
M13	**3.987 - 4.145**	**4.06**	**634**	**Dual**
M14	8.407 - 8.748	8.58	336	Single
M15	**10.234 - 11.248**	**10.74**	**343**	**Single**
M16	11.405 - 12.322	11.86	340	Single
DNB	**0.5 - 0.9**	**0.7**	**0.0186**	**Triple**

[1]Units are $W{\cdot}m^{-2}{\cdot}sr^{-1} \cdot \mu m^{-1}$ for M7, M8, M10; K for M12-M16; $W{\cdot}cm^{-2}{\cdot}sr^{-1}$ for the DNB.

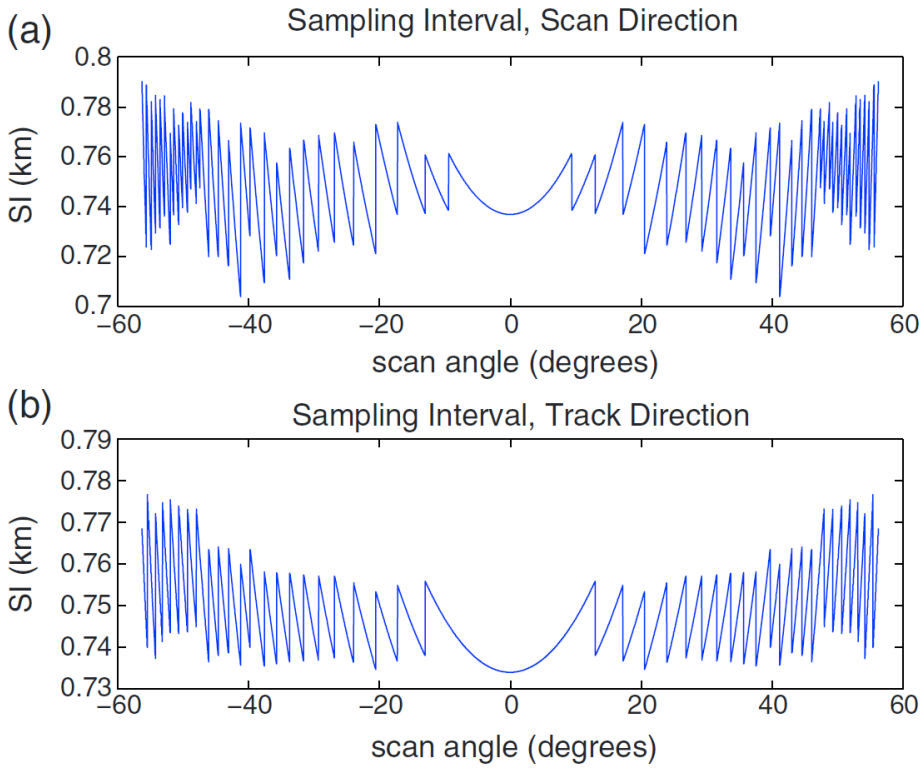

Figure 3.1: Horizontal sampling interval for the DNB. (a) is in the scan direction, (b) is in the track direction. The DNB employs 32 symmetric off-nadir aggregation zones to maintain a near-constant pixel footprint. Adapted from (Liao et al., 2013).

between the four focal plane arrays on-the-fly. In addition to its wide dynamic range, the DNB also features a nearly constant IFOV across the swath, accomplished by employing 32 different aggregation zones for its 672 time-delay-interval (TDI) detectors (Liao et al., 2013), as seen in Figure 3.1. Figure 3.2 illustrates the aggregation modes for two pixel locations, nadir and the edge of scan (EOS). At nadir, the 672 detectors scan the earth, and 42 detectors are aggregated to comprise each of the 16 pixels per scan. At the EOS, due to the growth of the detector footprint, only the central 320 detectors are aggregated to form the 16 pixels (20 detectors per pixel). Thus, the DNB is geolocated with the M-bands only at nadir; otherwise, the DNB and M-bands grow at very different rates, as explained by their independent aggregation modes.

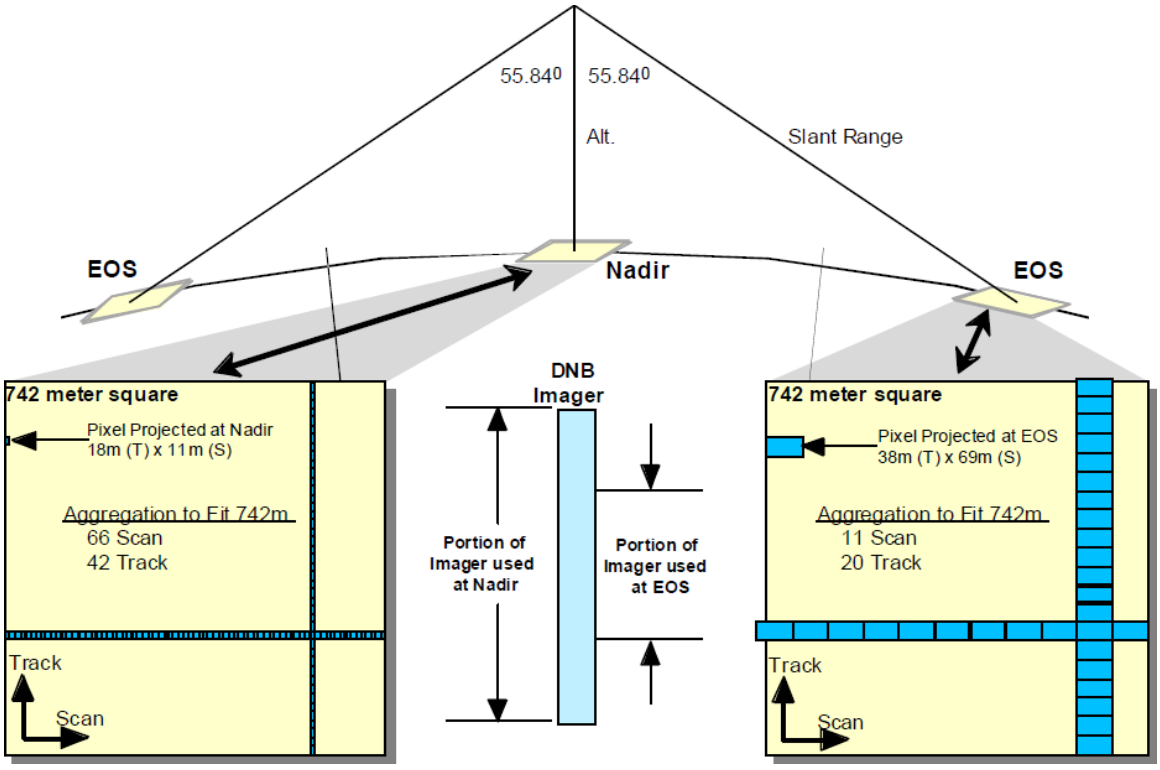

Figure 3.2: Illustration of the DNB aggregation technique for one pixel. Adapted from the VIIRS Geolocation ATBD (JPSS, 2011b).

3.2 ASTER

In order to evaluate our proposed algorithm, a different sensor with a higher spatial resolution to observe smaller fires must be used. Many past fire studies have opted to use airborne sensors such as the Airborne Infrared Disaster Assessment System (AIRDAS) as in Ambrosia et al. (1998) or the Autonomous Modular Sensor (AMS) like in Peterson et al. (2013), due to several reasons. These include their extremely high spatial resolutions, the reduced severity of atmospheric contamination, and ability to plan coincident overpasses. There is no supplemental airborne dataset to compare with VIIRS data, unfortunately; thus, a different spaceborne sensor needed to be utilized. The Advanced Spaceborne Thermal Emission and Reflection (ASTER) instrument aboard NASA's Terra satellite proved to be the best option. ASTER is capable of supplying 90 meter thermal infrared data at night in five bands across

a 60 km swath with a descending equator local crossing time of 10:30 AM. Using 12 bit quantization, it supports a 4.2 mbps data rate to relay the information sensed by its ten Mercury-Cadmium-Tellurium detectors. The longwave bands must be used, as the shortwave infrared and visible data collection is turned off for nocturnal scenes. Unfortunately, longwave emissive bands are much less sensitive to fires than shorter wavelengths as described by the Planck function, so ASTER's shortest TIR band, B10—spanning 8.125–8.475 μm—is utilized. This channel is sensitive to water vapor, but there is still a substantial fire signal nonetheless when compared to background radiation. ASTER data is available for free in the HDF4 file format.

Selecting a scene with a coincident VIIRS and ASTER overpass is challenging since nighttime ASTER data is sparse, and the odds of jointly overpassing a fire event are slim. Manual perusal of the ASTER database is necessary as a result; however, the United States Geological Surveys Global Visualization Viewer (GLOVIS) website assists in visualizing the ASTER data and identifying scenes containing fires. It was soon discovered that ASTERs packaged geolocation tie-points were consistently mismatching the true geolocation by up to two tenths of a degree, so the data are manually projected using the SceneFourCorners metadeta, which is outlined in the ASTER data handbook (http://asterweb.jpl.nasa.gov/content/03_data/04_Documents/aster_user_guide_v2.doc). A quick description of the process is outlined below:

1. Retrieve the latitude and longitude of the top leftmost pixel, the map orientation angle, and the Universal Transverse Mercator (UTM) zone for the ASTER scene.

2. Project the top left corner forward into UTM projected space using a WGS 84 ellipsoid.

3. Determine the latitude and longitude for each of the remaining pixels, factoring in the map orientation and spatial resolution of the band.

Once an ASTER scene is found containing a fire, a corresponding VIIRS scene is obtained. This is significantly easier than its ASTER counterpart due to the large size of the VIIRS swath and its orbital characteristics.

Chapter 4

Methods

Due to the different aggregation schemes and differing IFOVs between the DNB and M-bands, VIIRS data need to be processed in several ways before they can be used in the fire detection algorithm. In addition, further processing is needed to account for pixel overlap, despite the on-board overlap deletion (bow-tie deletion). We first describe these procedures and then discuss the VIIRS fire algorithm and our modifications to it.

4.1 Data Processing

Correcting for the scan overlap due to the Earth's curvature is the first obstacle, and the aggregation scheme for the M-bands makes this increasingly complicated. The effect is most pronounced near the edge of the scan and before the switch between each aggregation regime. While viewing fires from different geometries can be advantageous, it artificially inflates fire retrievals. Therefore, to avoid spuriously double-counting fire pixel detections, overlapping pixels are removed by exploiting the similarities in VIIRS scans. The method is similar to that in (Peterson et al., 2013), only it is applied to VIIRS instead. One M-band VIIRS scan consists of 3200 along-scan pixels and 16 along-track pixels; however, to accommodate

aggregation, each scan is actually comprised of 6304 along-scan samples by 16 along-track samples. In order to make the overlap calculation feasible, the sample dimensions are first determined using VIIRS geometry and assuming the Earth is a perfect sphere without terrain influences. Samples that overlap the subsequent scan's track samples for more than 50% of their area are then excluded. Afterwards, the non-overlapping samples are aggregated into pixels according to VIIRS specifications. This resultant exclusion "mask" is then applied to the data for each VIIRS scan, and since each scan follows the same scanning geometry, it can be quickly applied to the entire data segment (granule). After overlap correction, for one scan, only 7 rows of along-scan pixels suffer from no overlap by the edge of the scan; the remaining 9 rows experience some degree of overlap. For perspective, 13% of a given VIIRS granule has some overlap deleted onboard the satellite to reduce downlink bandwidth requirements (bow-tie deletion). After manually correcting overlap, an additional 11% is removed; thus, a total of 25% of the granule's pixels are removed due to overlap.

Figure 4.1, picturing the Souris River in North Dakota with a viewing zenith angle of $\sim 60°$, shows the same sequence of scans before and after correcting for pixel overlap. The black lines in Figure 4.1a are the bow-tie deleted areas, which is done onboard the satellite according to VIIRS data processing procedures (JPSS, 2011b). As seen by the repeating river pixels circled in red, it is clearly imaging the same area twice, despite the bow-tie deletion. Figure 4.1b shows the individual pixel footprints when the same region is enlarged, highlighting the need for overlap correction. Figure 4.1(c) and (d) shows the resulting scene after correction, with minimal resulting gaps or overlap.

After correcting for pixel overlap, normalizing the DNB to M-band pixel sizes is necessary due to their different aggregation schemes and IFOVs. Similar to overlap correction, this approach employs the similarity of VIIRS scans to quickly match the DNB to the M-bands. First, one scan of 16 along-track pixels is analyzed. Since VIIRS is polar-orbiting with an inclination of 98.7°, as the satellite descends in its nighttime orbit, the primary along-scan

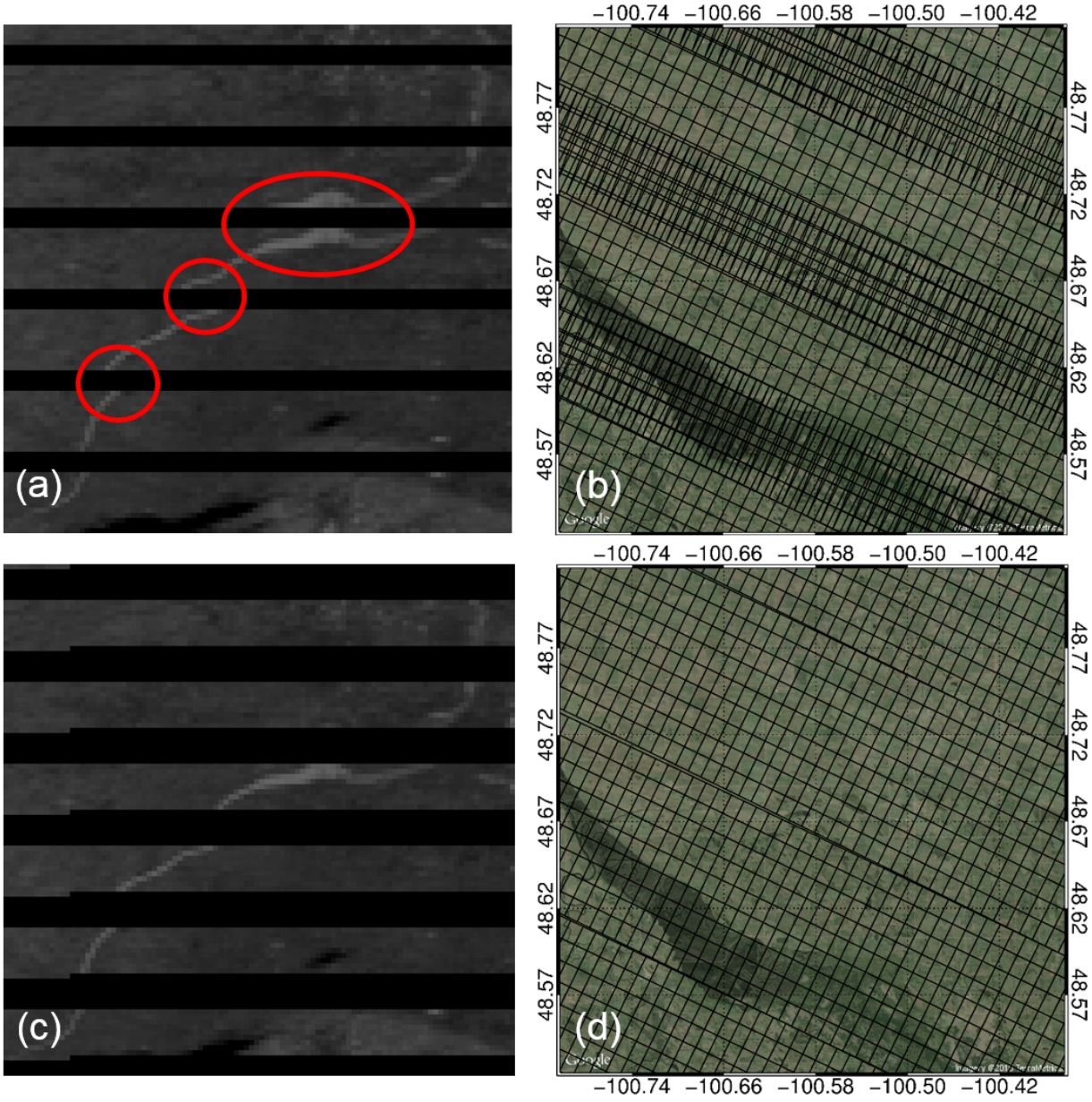

Figure 4.1: Correcting for pixel overlap. (a) shows the VIIRS un-projected M13 (BT_4) scene before corrections. The red outlines highlight the duplicated river areas. (b) shows the pixel footprints for the M13 VIIRS scene before corrections. (c) and (d) show the same images after corrections. Without overlap correction, the same pixel is often counted twice near the edge of the scan.

axis of change is the longitude (excluding extremely high latitudes, which fortunately do not have many fires). Pixel longitudes are taken from the the M-band terrain-uncorrected geolocation, since there is no DNB terrain-corrected geolocation available for the study period. For each M-band pixel, the left and right edge longitudes are determined by taking the midpoint between neighboring pixels, and then the DNB pixels that fall within that M-band pixel's edges are averaged based on the respective DNB pixel longitude edges. DNB pixels that lie between two M-band pixels have their respective fractions combined into the appropriate M-band pixel. However, since there is still considerable M-band footprint growth in the along-track direction far from nadir (and not in the DNB), they must also be combined in the along-track direction as well using the same principles. After this has been done for one full scan, the calculated geometry and fractions are then used to correct the remaining scans in the granule. Terrain-corrected geolocation can then be utilized for the M-bands/DNB from this point forward.

4.2 The VIIRS Fire Detection Algorithm

Currently, the VIIRS fire detection algorithm (called the Active Fire Application Related Product, or AFARP) is based almost exclusively on the MODIS fire detection algorithm presented by Giglio et al. (2003), which is the equivalent of the MODIS Collection 4 (JPSS, 2011a; Csiszar et al., 2013). As mentioned in Chapter 2, the algorithm is tuned to be conservative and reduce false positives.

The nighttime version of the algorithm, presented in Figure 4.2, begins by using an internal cloud mask to filter out pixels with a BT_{12} (M16) less than 265 K. In addition, any pixels that are known to be water (based on a static database) are filtered out, and any pixels with missing or invalid data are removed. Afterwards, the algorithm selects pixels that could be fires, which is any unfiltered pixel with a $BT_4 > 305$ K and $BT_4 - BT_{11} > 10$ K.

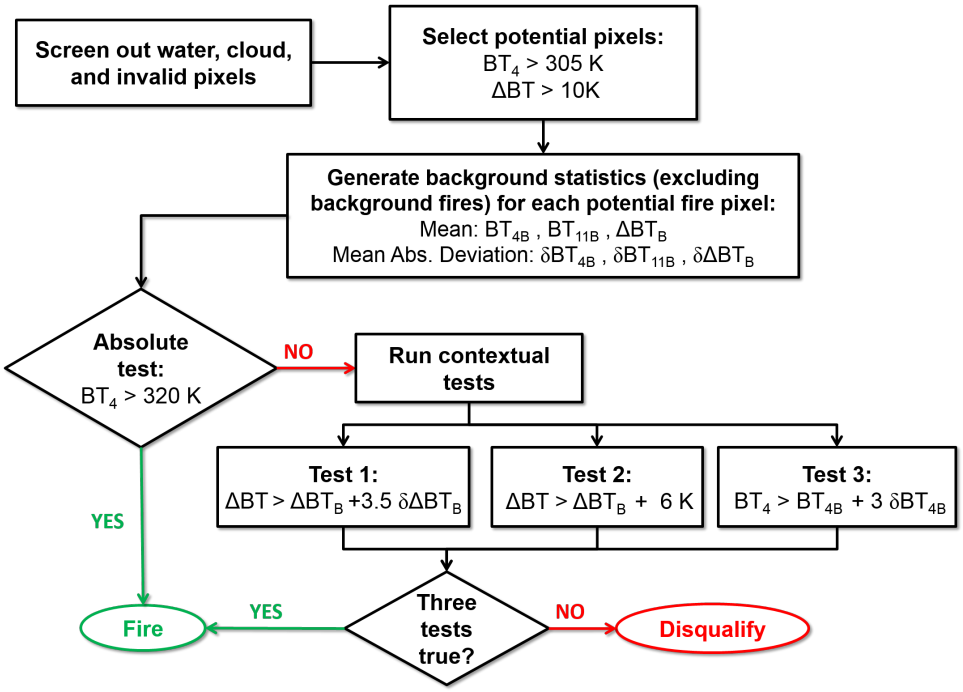

Figure 4.2: The nocturnal VIIRS operational fire detection algorithm, which is based on Giglio et al. (2003)—e.g. MODIS Collection 4. If the tests pass, the pixel passes along green lines, whereas if they fail, they follow the red lines. Pixels must either pass the absolute test or all three contextual tests in order to be flagged as a fire.

If any pixels meet those criteria, they have their background statistics calculated, analyzing the pixel's environment relative to neighboring pixels. The background statistics include the calculation of the mean, median, standard deviation, and the mean absolute deviation—used due to its insensitivity to outliers (Huber, 1972)—by an expanding 3×3 grid centered on the pixel. The grid continually expands until at least 25% of the included pixels are valid, meaning they have a $BT_4 < 310$ K and a $BT_4 - BT_{11} < 10$ K (e.g. not a background fire pixel), are not cloudy, and are land, with a minimum of 8 pixels in total (Giglio et al., 2003). If the grid's size reaches 21×21 pixels, the individual pixel it is centered on is flagged as *unknown*. Once the statistics are generated for each potential fire pixel, then four tests are applied to the pixel to determine if it is a fire. The first test is the "absolute" test, and the pixel is flagged as a fire if $BT_4 > 320$ K. If the pixel does not pass the test, then the other

three contextual tests are applied, and a pixel must pass all three to be flagged as a fire. They are:

1) $\Delta BT > \Delta BT_B + 3.5\delta(\Delta BT_B)$

2) $\Delta BT > \Delta BT_B + 6$ K

3) $BT_4 > BT_{4B} + 3\delta BT_{4B}$,

where ΔBT is $BT_4 - BT_{11}$, ΔBT_B is the background $BT_4 - BT_{11}$, $\delta(\Delta BT_B)$ is the background mean absolute deviation of $BT_4 - BT_{11}$, BT_{4B} is the mean background BT_4, and δBT_{4B} is the background mean absolute deviation for BT_4. During the daytime, there are additional tests to disqualify pixels due to sun glint, unmasked water pixels, and deserts, but they require solar reflectivity and are not utilized at night (Giglio et al., 2003). After the fire pixels have been identified, they are logged. The VIIRS fire product, known as the Active Fire Application Related Product (AFARP), contains the columns and rows, latitudes and longitudes, and the quality flag data for each fire pixel. Non-fire or disqualified potential fire pixels are not included in the product. Although MODIS Collection 4 is now obsolete, VIIRS is able to overcome some of its shortcomings due to its improved spatial resolution. However, despite the improved spatial resolution, it still relies on a pre-specified 4 μm BT threshold of 305 K for potential pixel selection, omitting smaller and cooler fires, irrespective of the environment they are located in.

4.3 The FIreLight Detection Algorithm (FILDA)

Our approach is similar to that of Giglio et al. (2003) and JPSS (2011a) with three important differences. First, instead of relying on a pre-specified BT_4 threshold of 305 K, FILDA generates the BT_4 dynamically for each VIIRS granule. Second, visible light is also included in the potential fire pixel selection process. Lastly, we do not screen out water pixels in order to capture gas flares and other phenomena such as island volcanoes, since sun glint is not an

issue at night. The basis for this methodology is that pixels with visible light emission and 4 μm BT signatures are likely to be fires (or volcanoes in some cases).

Initially, FILDA and AFARP begin nearly the same, and they screen out invalid pixels such as clouds, though this approach does consider water pixels. An added step for FILDA is also filtering out pixels with a solar zenith angle less than 100°, fully removing all twilight areas. Afterwards, the overlap correction is applied, and the DNB is collocated with the M-bands. Next, unlike in AFARP, the BT thresholds for potential fire pixel selection are calculated by binning the remaining pixels' 4 μm BTs for the granule in increments of 1 K and then selecting the lowest bin of the hottest 0.5% as the 4 μm threshold. For example, a granule containing most of the West Coast of the U.S. on 24 August, 2013 has a median 4

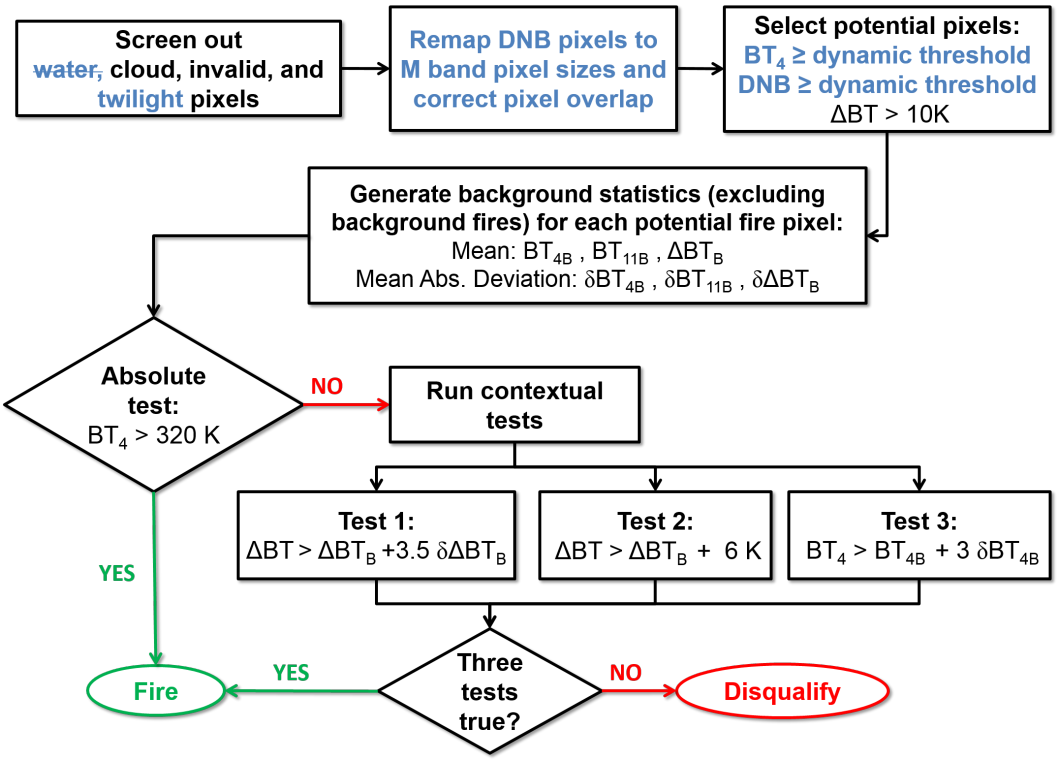

Figure 4.3: Flowchart of FILDA, the FIreLight Detection Algorithm used in this study, which is based on the operational nocturnal VIIRS fire product (AFARP). Blue text highlights modifications to the algorithm in contrast to Figure 4.2.

μm BT of 283 K. When binned into 1 K increments, the relative frequency drops off radically after 298 K, as seen in Figure 4.4. The resulting BT_4 threshold in this example is then 298 K. Similar to the 4 μm BT threshold, the DNB threshold is calculated in an identical way, binning into increments of 1 nW·cm^{-2}·sr^{-1}—except using the top 0.1% instead of 0.5%. In the same Western U.S. example, the resulting DNB threshold is 15 nW·cm^{-2}·sr^{-1}. In most cases, the DNB threshold is primarily influenced by moonlit terrain and low-level clouds not screened by the internal cloud mask due to their higher BTs.

Other thresholds varying from 0.5% to 0.01% were investigated for both the BT_4 and DNB thresholds. The top 0.5% threshold for BT_4 generally reflected the precipitous decline in frequency the ∼50 cases examined. Reducing the BT_4 threshold to 0.01% made it increasingly insensitive to granule variation, with most BT_4 thresholds in warm regions not much lower than AFARP's static BT_4 threshold of 305 K. For perspective, the top 0.5% of a standard 3200×3072 pixel VIIRS granule (9.83×10^6 pixels) adds a startling 49,152 pixels to the potential fire pixel selection process, accounting for large thermal variation. However, when coupled with the DNB's threshold using the top 0.1% brightest, the maximum number of potential fire pixels is reduced to 9,830, even before the ΔBT threshold is considered. In the above example (Figure 4.4), there are only 173 potential fire pixels in the granule which meet all of those criteria, of which 169 pass contextual tests (this granule was taken during a night of intense burning over the Rim Fire).

The end result of the change in potential fire pixel selection criteria is that the potential pixels must have three properties: they are among the 0.5% hottest pixels, they are also among the 0.1% brightest pixels in the DNB, and lastly, they must all have a ΔBT of at least 10 K. In the case that a pixel is hotter than 305 K in 4 μm without meeting the DNB threshold, it is still marked as potential fire pixel just as in AFARP, however (assuming $\Delta BT > 10$ K). For example, using the data from Figure 4.4, if a pixel has a $BT_4 = 299$ K, a DNB value= 16 nW·cm^{-2}·sr^{-1}, and $\Delta BT = 12$ K it would be considered a potential

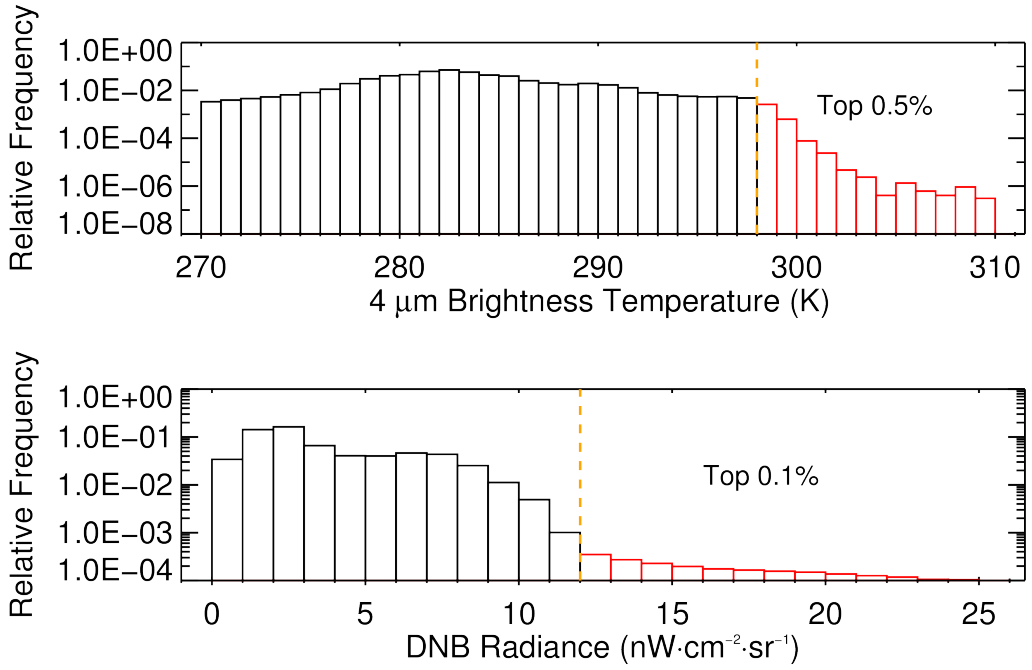

Figure 4.4: Histograms of valid 4 µm BTs and DNB radiance values for the nighttime 24 August, 2013 granule of the Western United States (orbit 9449). The orange dashed line represents the thresholds calculated for this granule. Red rectangles indicate bins that exceed the threshold requirement and are included in potential fire pixel selection.

fire pixel; however, if the DNB radiance value is 14 nW·cm^{-2}·sr^{-1} instead, it would not be considered as one. Likewise, if a pixel has a $BT_4 = 294$ K, $\Delta BT = 11$ K, but a DNB value of 25 nW·cm^{-2}·sr^{-1}, it would also not be considered as a potential fire pixel. But if the BT_4 was 308 K, $\Delta BT = 11$ K, and DNB=7 nW·cm^{-2}·sr^{-1}, it would be considered a potential fire pixel and analyzed further.

After the identification of potential fire pixels, FILDA proceeds exactly as AFARP by running the same absolute and contextual tests. No additional tests are added. At the end, fire pixel latitudes, longitudes, columns, and rows are logged.

Chapter 5

Results

Several case studies are presented to show FILDA's potential of using visible light at night to improve fire detection, ranging from large forest fires to gas flares. They are chosen based on three factors: 1) environmental variety representation, 2) availability of coincident ASTER overpasses, and 3) the impact level of the fire. Here, we examine California's Rim Fire, which burned in the summer of 2013; the High Park Fire in Colorado from the summer of 2012; and gas flares in the Khanty-Mansiysk and Niger Delta regions from the summer and winter of 2013, respectively.

5.1 The Rim Fire

Located by Yosemite National Park in the Sierra Nevada Mountains in California, the Rim Fire was the third largest wildfire in California's history. It was ignited at 3:25 PM (local time) on 17 August 2013 by a hunter's illegal campfire, and while it grew slowly at first, the fire grew explosively a week after ignition. The Rim Fire's rapid growth was primarily driven by favorable upper air conditions, which created sustained low relative humidities and strong winds near the surface, especially during nighttime hours (Peterson et al., 2014). By

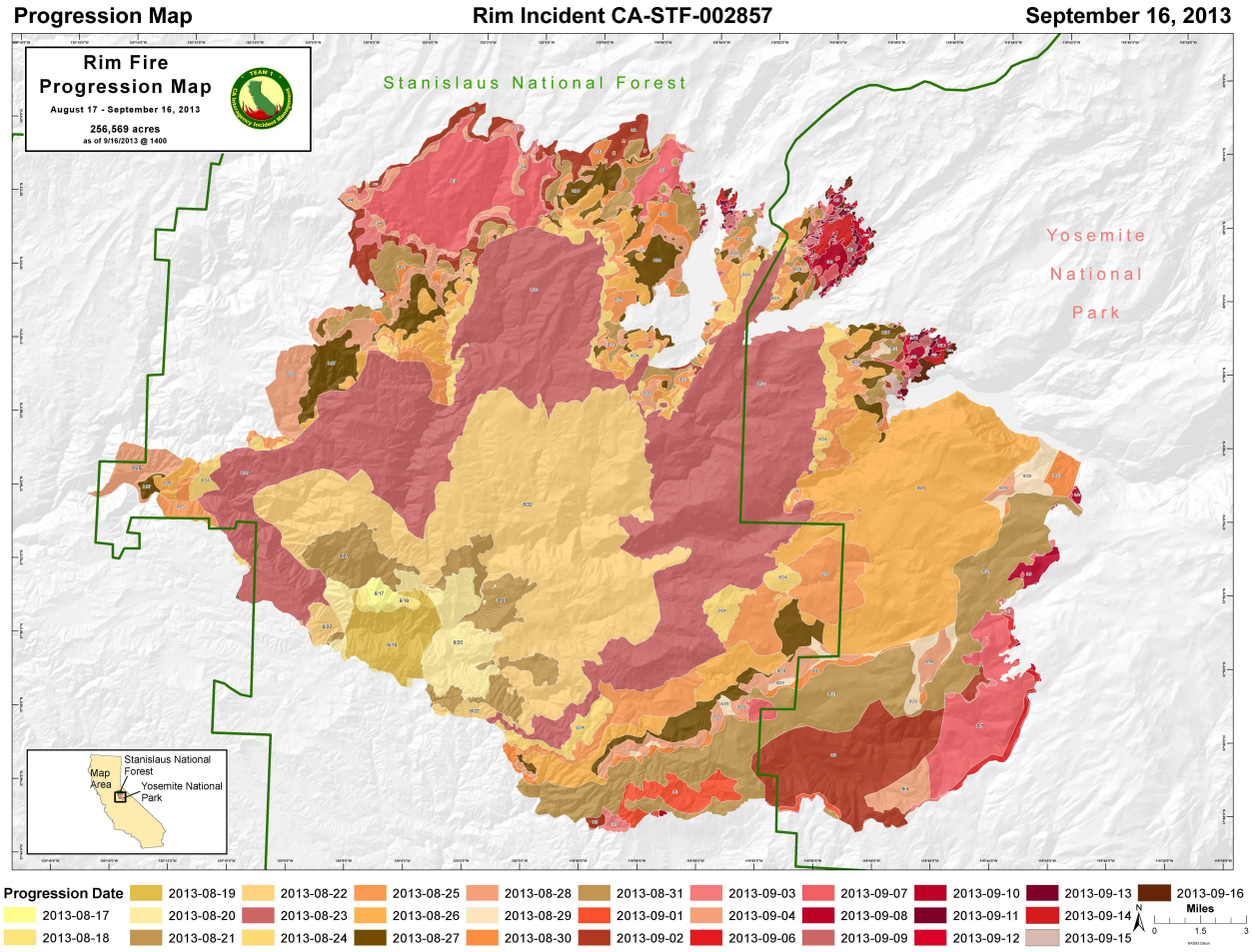

Figure 5.1: Rim Fire estimated progression map created by the U.S. Forest Service using airborne NIROPS data. (http://inciweb.nwcg.gov/incident/map/3660/1/)

the time it was extinguished, it had burned over 250,000 acres of forest within one month.

The U.S. Forest service closely monitored the progress of the Rim Fire with the National Infrared Operations (NIROPS) program, which is employed when there is a significant fire hazard to life and property. NIROPS supplies high-resolution infrared data taken from nighttime aircraft flights and serves to monitor the movement of the fire front. The data are not publicly available, unfortunately; however, the Forest Service does use NIROPS to construct publicly-available fire progression maps. Figure 5.1 is one such map; it shows the progression of the Rim Fire up to 16 September 2013, a week before it was finally

extinguished. While the full progression of the Rim Fire is not present, it did not grow significantly beyond this date. The map will serve as a baseline for comparison of VIIRS fire detections.

VIIRS provides a unique vantage point to study the Rim Fire because of its ability to track the smoke and light emissions at night. Because the fire continued to grow quickly during nocturnal hours, the Rim Fire is an ideal candidate for FILDA application. After applying FILDA to every VIIRS scene covering the Rim Fire during its burn duration (48 granules), Figure 5.2 shows the comparison between AFARP (left) and FILDA (right) fire pixel detections. The first major difference between the two is that FILDA is able to detect the Rim Fire the first night it burned, with an overpass time of 2:43 AM PDT on 18 August 2013. AFARP is unable to identify the fire because the pixel's 4 μm BT is only 301.7 K, which is 3.3 K below the minimum detection threshold. Meanwhile, FILDA's 4 μm BT threshold is 298 K with a DNB threshold of 10 $nW \cdot cm^{-2} \cdot sr^{-1}$. Comparing the two maps, a distinct pattern can be seen: the growth of the Rim Fire is much more defined using FILDA. FILDA's progression map also much more closely resembles that of Figure 5.1, with similar patterns despite the aircraft's variance in flight times. The large gaps in coverage for both images occur due to a period of explosive growth between 3:27:26 AM PDT on 21 August 2013 to 3:04:14 AM PDT on 22 August 2013, during which the fire tripled in area burned.

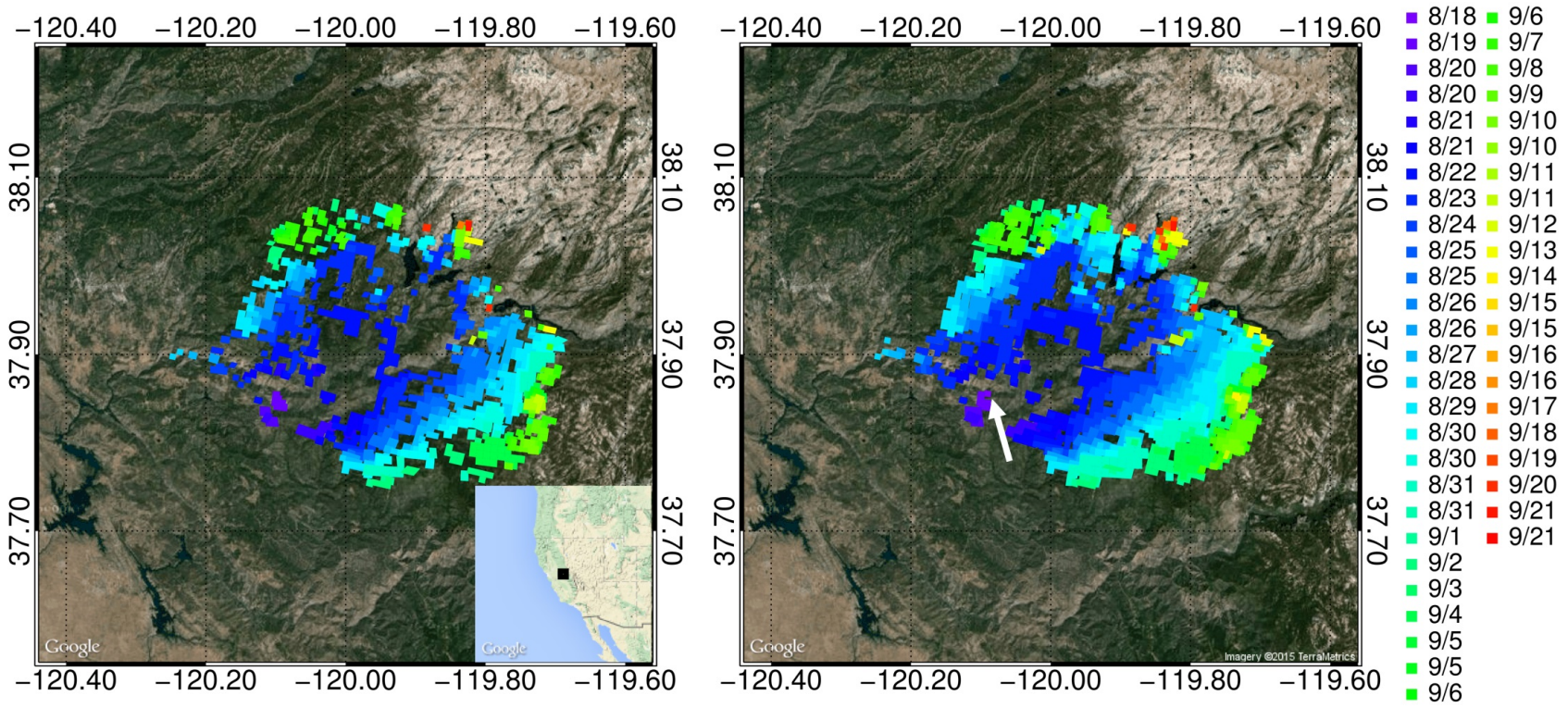

Figure 5.2: Progression of the Rim Fire from ignition to extinction. The left panel shows the Rim Fire's development using AFARP, while the right panel shows the fire's progress using FILDA. The white arrow highlights the first nocturnal detection by VIIRS using FILDA at 2:43 AM PDT on 18 August 2013, 11 hours after ignition. AFARP was not able to identify the fire at night until 19 August. Some days are repeated due to consecutive overpasses.

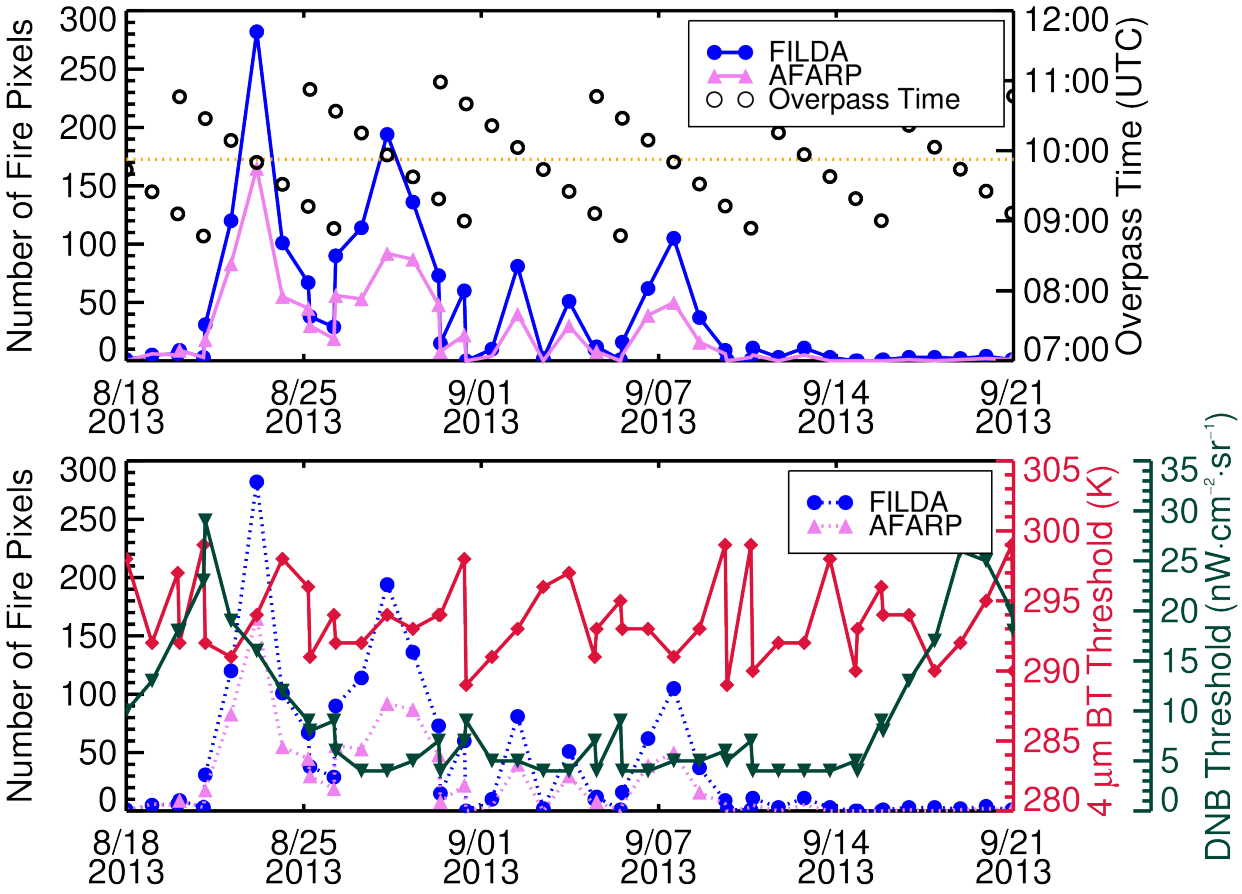

Figure 5.3: Time series of fire pixel counts as they relate to overpass time (top) and thresholds (bottom). FILDA pixel counts are displayed in blue, while AFARP counts are shown in gold.

As mentioned, FILDA's BT_4 and DNB thresholds are dynamic for each VIIRS swath. Figure 5.3 shows how the pixel counts and thresholds vary with each scene and scanning geometry. The top graph relates the pixel counts for FILDA and AFARP in relation to scan angle; as with any other scanning radiometer, geometry plays a significant role in retrievals. Near-nadir cases are closest to the orange dotted line. These nadir cases show obvious peaks in fire pixel retrievals, both for FILDA and AFARP, since there are more pixels encompassing the fire region. Farther from nadir, fire pixel frequencies are somewhat reduced. It should be

noted that this effect will be smaller than for MODIS because of the reduced pixel footprint growth rate due to the VIIRS aggregation scheme. The bottom graph shows how the BT_4 and DNB thresholds vary with each scene. Overall, the BT_4 threshold varies between ∼290 K and ∼300 K; note that the very top of the 4 µm axis is the threshold for AFARP.

Rapid shifts in overpass time reflect that the Rim Fire has been scanned twice in one night due to being close to the scan edge in two consecutive orbits. In those situations, a large difference in BT_4 thresholds is apparent. This occurs because the second scene is primarily comprised of ocean pixels, which have a much lower average BT_4 than land. For example, the first scene from 31 August 2013 has a BT_4 threshold of 298 K, as the swath contains most of the western United States and the northern part of Mexico. Conversely, the second swath images mostly ocean pixels with the exception of California—and the cool Pacific Ocean waters skew the threshold to a cooler value. This causes a slight artifact of increasing FILDA fire pixel retrievals for the ocean scene, as the BT_4 threshold is lower, as evidenced by 31 August 2013's FILDA retrievals, which are nearly doubled between scenes. However, most increases are modest and not extreme. Unlike the BT_4 threshold, the DNB threshold is primarily governed by the lunar cycle. This is because moonlit terrain effectively raises the signal floor, increasing the minimum DNB radiance for the top 0.1%. For moonless or nearly-moonless scenes, the top 0.1% instead captures the effects of artificial lights.

The algorithm is also evaluated by studying the Rim Fire on 24 August 2013, which had a coincident ASTER overpass. The Rim Fire was imaged the night immediately after its second day of explosive growth, during which it doubled its area burned from the day before. The explosive growth left large swaths of smoldering vegetation in its wake. Figure 5.4 shows a multi-band view of the Rim Fire that night, as well as the ASTER imagery. Figure 5.4a shows the pixel locations overlaid onto Google Earth satellite imagery. The blue boxes represent FILDA pixels, whereas the golden boxes are the AFARP pixel locations. In this scene, every AFARP pixel is also independently identified as a FILDA pixel. The rest

of the panels (b-e) show the Rim Fire at different wavelengths. Panel (b) is the VIIRS 4 μm band (band M13), and the fire front is easily discernible. AFARP captures the most intense fire hotspots, but much of it is ignored; FILDA, on the other hand, shows a more continuous fire front. Panel (c) is ASTER's 8.3 μm band, which also shows the fire front hot spots at a much finer resolution. ASTER imaged the Rim Fire 3.5 hours before VIIRS did; while the ASTER band shows a tendency to slightly emphasize smoldering terrain, it still identifies the fire front quite well. It also reminds us that fire events are entirely sub-pixel in nature, even in large fire complexes such as this Rim Fire scene. Panel (d) is the DNB image, which makes two important points: 1) it is correlated with the 4 μ band, and 2) it is useful for identifying smoldering terrain. This is seen in the terrain left behind after the fire front has passed; some of it is even identified as fire pixels by FILDA. Lastly, the VIIRS I4 band (centered at 3.7 μm) is shown in panel (e). The increased spatial resolution highlights the terrain effects as well as smaller flare-ups not well-observed in the moderate-resolution 4 μm band. Unfortunately, there are two I4 pixels that saturate in this scene and appear as missing data. They have been marked with the two purple arrows, as they are hard to identify.

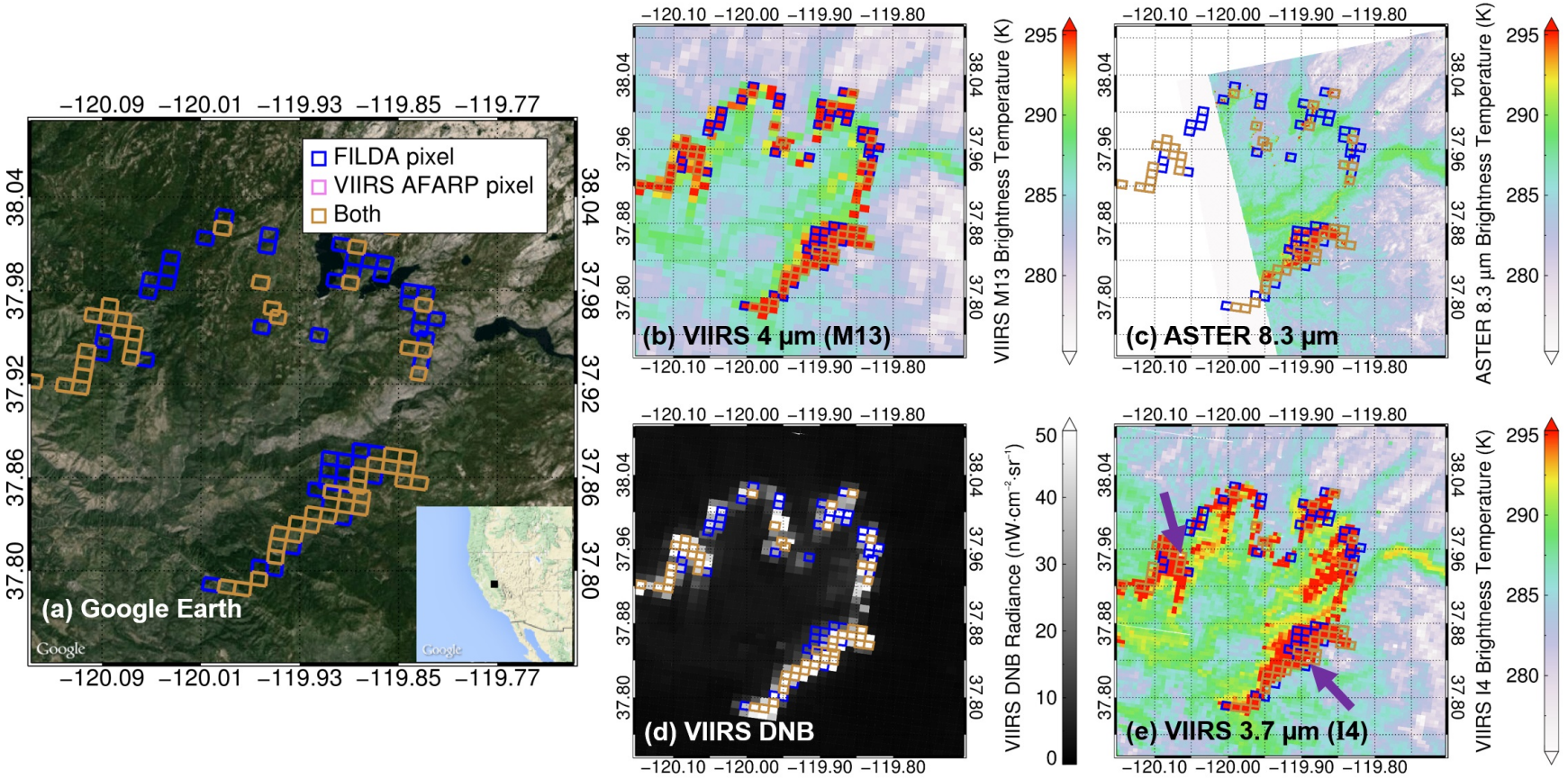

Figure 5.4: Multi-band/sensor view of the Rim Fire taken at 2:29 AM PDT on 24 August 2013 by VIIRS. ASTER [panel (c)], aboard Terra, scanned the fire at 11:01 PM PDT on 23 August 2013. The blue boxes are pixels detected by FILDA, whereas the gold boxes are from AFARP. Note that FILDA also included all AFARP pixels. The purple arrows in (e) point to saturating pixels in the I4 band.

The VIIRS 24 August 2013 scene is further analyzed to show the method by which FILDA operates. A two-dimensional histogram of DNB radiances versus 4 μm BTs for the entire granule is presented in Figure 5.5, binned into increments of 1 nW·cm^{-2}·sr^{-1} (DNB) and 1 K BTs (4 μm). It shows which pixels are classified as fires by FILDA and AFARP. The dashed gold line indicates the 4 μm potential fire pixel BT threshold of 305 K used by AFARP as well as by FILDA when the DNB radiance is below the minimum DNB threshold. The solid blue line represents the threshold determined by FILDA. In this case, the threshold BT_4 threshold is 298 K, and the DNB threshold is 12 nW·cm^{-2}·sr^{-1}. Importantly, AFARP does not classify many of the potential fire pixels as fires, while FILDA does. There is no publicly-available diagnostic information for AFARP, so there is no method of identifying why and how the pixels are disqualified as fires. Secondly, there are many fire pixels with BTs less than 305 K, highlighting the need for reduced thresholds (preferably dynamically as in FILDA). Other case studies will show how the BT and DNB distributions change for each scene.

Several different populations of pixels are visible in Figure 5.5, marked by different numbers. They are presented as follows with decreasing occurrence. The major population in group (1) is comprised of low-altitude terrain, which reflects some moonlight, and then open Pacific Ocean water, which represents the lowest bins under the label (1). The (2) represents the majority of marine stratus clouds. Group (3) consists of a variety of features, which include high-altitude terrain like the Sierra Nevada Mountain Range and ranges in western Nevada and Central Oregon. It also contains pixels neighboring higher clouds, which stem from probable cirrus contamination. Lastly, some of the cooler marine stratus clouds are in this population. Group (4) varies widely in spatial distribution, but pixels are mostly non-arid locations like cities such as San Francisco and smaller towns. There are some highly reflective marine stratus clouds in this population as well, but it is primarily dominated by artificial lights. Group (5), conversely, is entirely comprised of arid/hot settlements and ar-

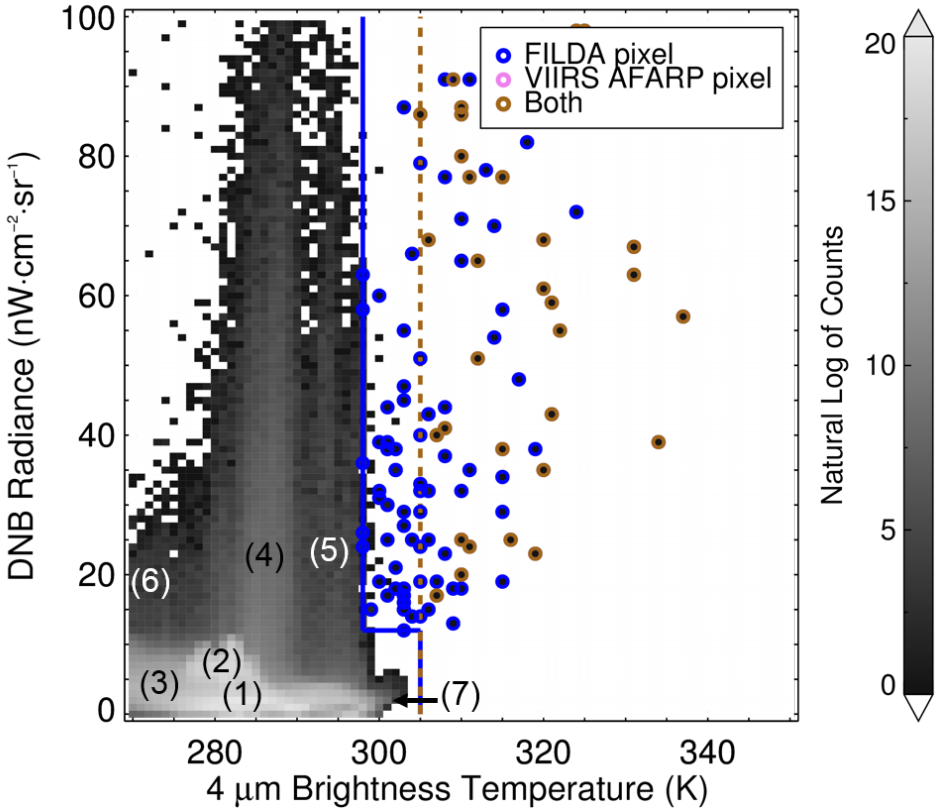

Figure 5.5: Two-dimensional histogram of the Rim Fire VIIRS granule used in Figure 5.4, showing fire pixel classifications for both FILDA and AFARP. In this case, every AFARP pixel is also a FILDA pixel. The blue line represents the FILDA thresholds, while the gold dashed line is the AFARP threshold. The annotated numbers describe each population of pixels: 1) most low-altitude terrain and open Pacific Ocean pixels; 2) marine stratus clouds; 3) high altitude terrain, cirrus clouds, and some cooler marine stratus clouds; 4) non-arid cities and towns, warm marine stratus clouds; 5) arid cities and towns; 6) cities under partial cloud cover; 7) desert environments.

tificial lights like Las Vegas and the urban heat island in Los Angeles. Group (6) is relatively uncommon and contains partially cloud-covered cities; the visible light penetrates the clouds, but they are attenuating the 4 µm signal. Lastly, group (7)—an unusual group—exists only in very warm areas. In this scene, only two places belong in this group: Death Valley and the waters of the Salton Sea, both located in Southern California. Though not marked as a

specific group, fires can be seen as the outliers in warmer BTs and brighter DNB values.

During the course of the Rim Fire, there were several periods of cloud cover from pyroconvection and frontal passages. Unsurprisingly, during those times, AFARP has trouble identifying fire pixels because of the attenuated fire signal in the 4 μm channel. The issue is further compounded by cloud cover reducing solar heating during the day, and when combined with an arbitrarily high potential fire pixel threshold, makes fires particularly challenging to detect. Cloud cover moving into the area on 3 September 2013 is one such case (Figure 5.6). AFARP is unable to detect any fire pixels, but remarkably—despite the less-than-favorable conditions—the Rim Fire can still be seen burning underneath the cloud cover. Similarly, FILDA is unable to see the fires burning beneath the clouds, but it is able to identify two fire pixels ($BT_4 = 300.4, 296.6K$) on the periphery of the cloud edge thanks to the reduced BT_4 threshold of 296 K.

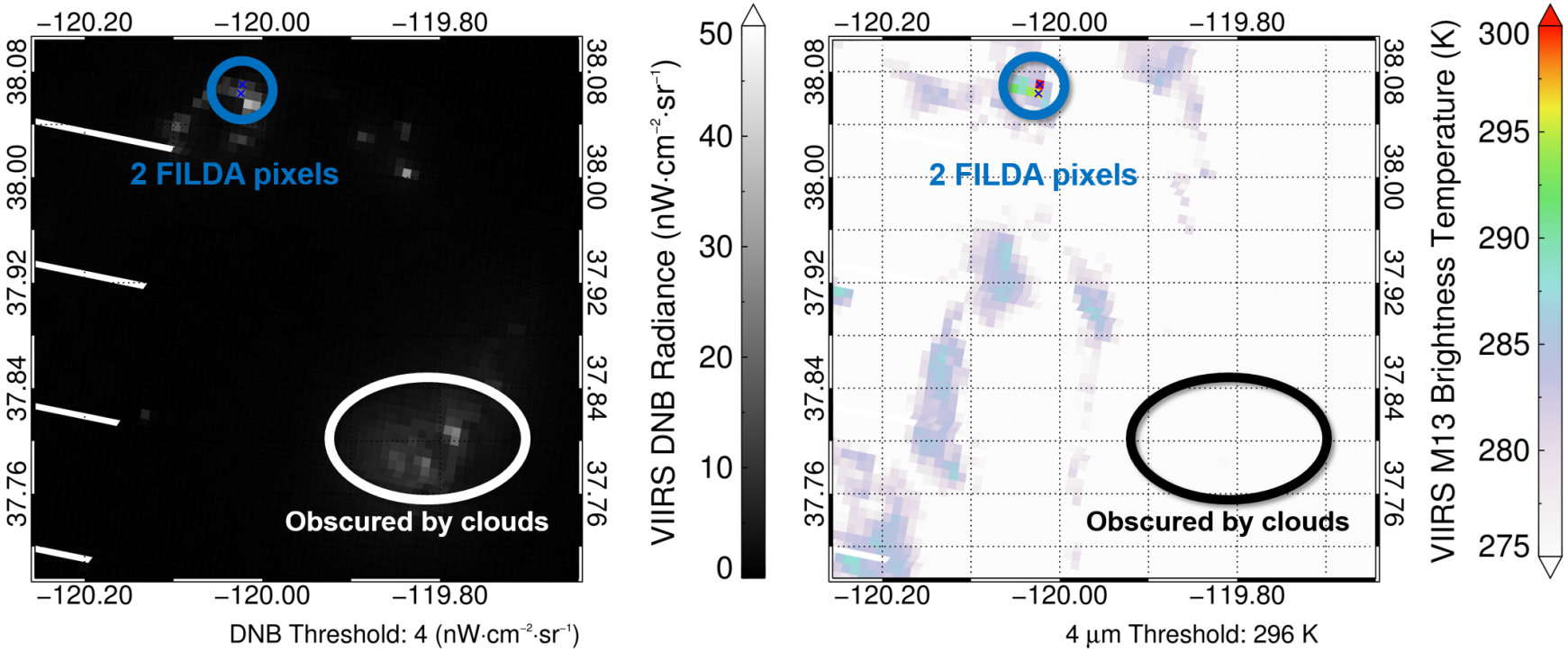

Figure 5.6: Imagery from 3 September 2013 showing the Rim Fire still burning underneath the cloud cover. AFARP could not identify any pixels, but FILDA identified two.

While the Rim Fire was an extremely dangerous and devastating fire, it provided the perfect opportunity to test FILDA and examine AFARP's performance due to its long burn duration and intense nighttime activity. In the remaining sections, we investigate a variety of other fires and apply FILDA to them.

5.2 High Park Fire

On 9 June 2012, lightning ignited a fire in the Roosevelt National Forest, near Fort Collins, Colorado (http://inciweb.nwcg.gov/incident/2904/). The fire burned for ∼21 days and scorched 87,000 acres before it was declared 100% contained on 30 June 2012. As the fire was located near Fort Collins, over 250 homes were destroyed, causing estimated damage and suppression costs of $39.2 million. Like the Rim Fire, it was a high-impact fire that burned intensely in excess of two weeks, making it another ideal candidate for FILDA. In this section, we only examine one day of observations, and not all of the observations over the course of the wildfire's lifespan.

The investigated nighttime period is 19 June 2012—primarily because that evening had a coincident ASTER overpass. Figure 5.7 shows the daily progression of the High Park fire from ignition until 22 June 2012. While the fire continued to burn for a week after the map was created, importantly it shows the movement of the fire on during the period of 18-19 June. Black arrows delineate the motion of the fire front westward, as much of the eastern front had been previously contained.

The panels in Figure 5.7 match up well with the Forest Service's NIROPS map on that night. ASTER scanned the fire event at 11:05 PM MDT on 18 June, with VIIRS overpassing the fire at 3:04 AM MDT on 19 June. While the four hour difference is significant, the High Park fire did not spread substantially during that period, and the same hot spots are still visible with both ASTER and VIIRS. FILDA identifies two intense and significant hot

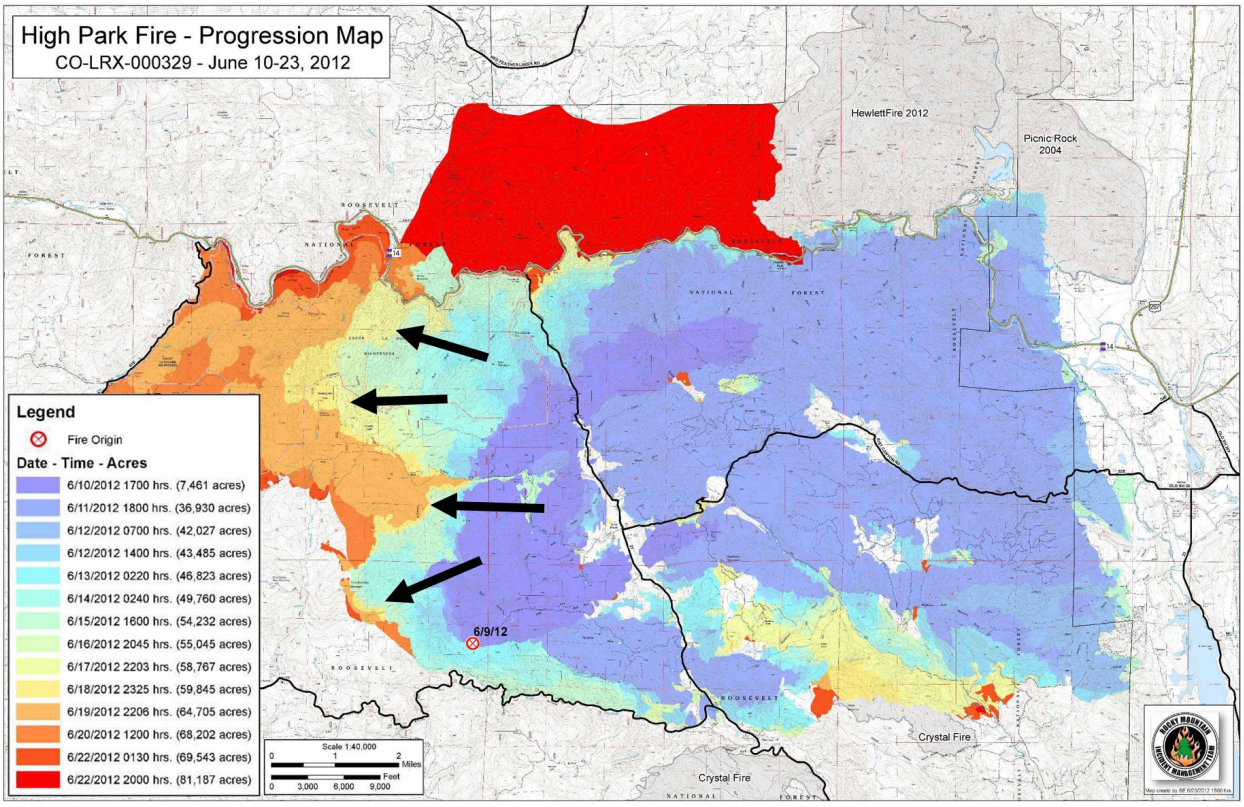

Figure 5.7: High Park fire estimated progression map created by the U.S. Forest Service using airborne NIROPS data, valid from 10 June 2012 to 22 June 2012, which includes the study scene. Black arrows indicate the progression of the fire front during the night of 19 June 2012. (http://inciweb.nwcg.gov/incident/map/2904/4/)

spot regions that AFARP neglected: the southernmost and northernmost portions of the fire. Instead, AFARP only flags the central portion of the fire front, highlighting its weak performance even with fires of moderate intensity and detracting from its usefulness for fire management.

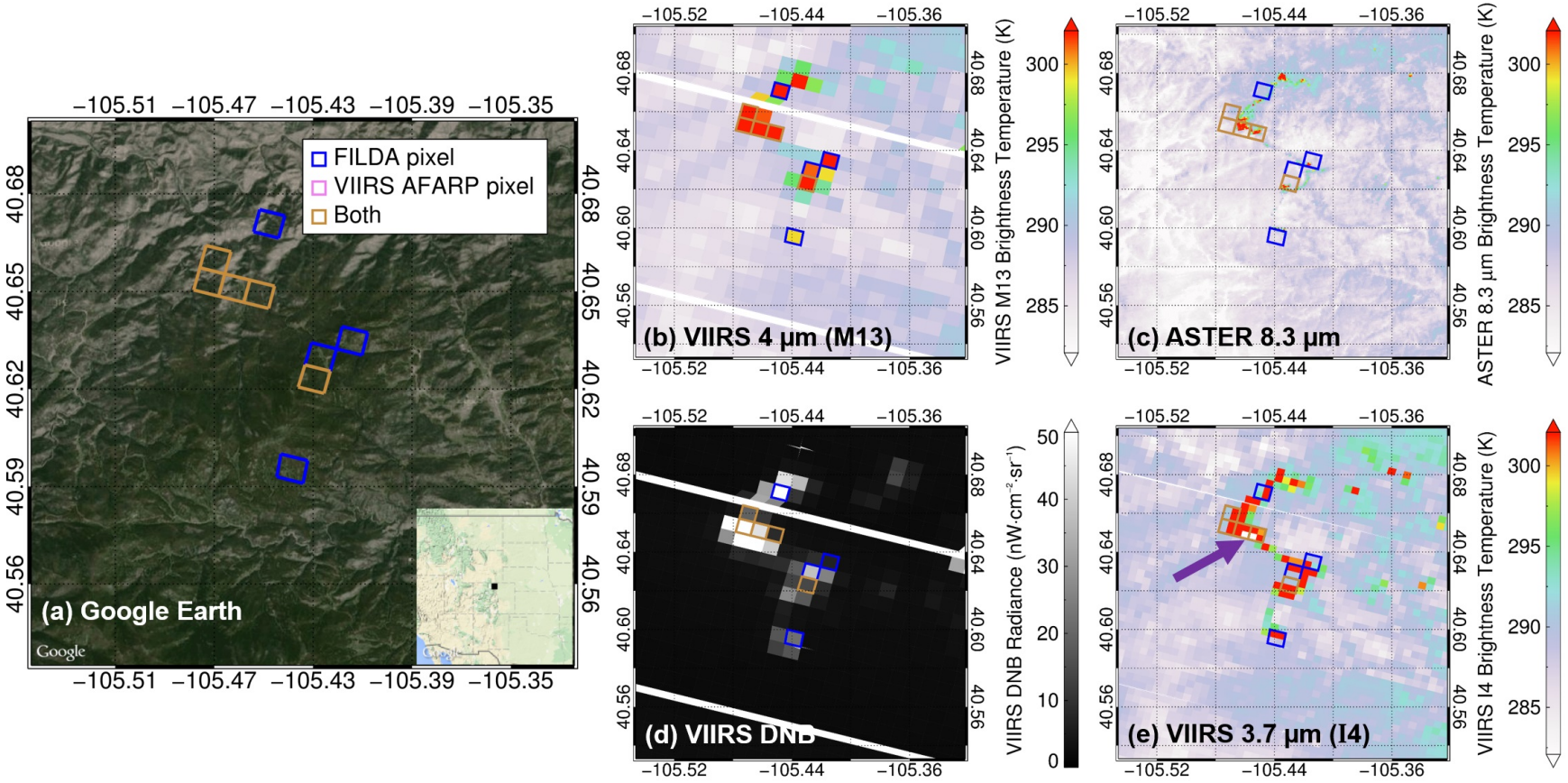

Figure 5.8: Multi-band/sensor view of the High Park fire taken at 3:04 AM MDT on 19 June 2012 by VIIRS. ASTER [panel (c)] scanned the fire at 11:05 PM MDT on 18 June 2012. The blue boxes are pixels detected by FILDA, whereas the gold boxes are AFARP detections. Note that FILDA also included all AFARP pixels. The purple arrow in (e) points to saturating pixels in the I4 band.

The reason behind its lackluster performance is easily discernible in Figure 5.9. With AFARP's minimum BT_4 threshold of 305 K, the majority of fire pixels are discarded before any analysis is done (e.g. anything to the left of the dashed gold line). To the contrary, FILDA determines the minimum BT_4 threshold should be 293 K for the scene, which encompasses these missed hot spots while successfully excluding most of the non-fire pixels. However, even FILDA does not classify some of these obvious hot spots as fires because they either fail the background tests or have a $\Delta BT < 10$ K, showing the difficulty of fine-tuning fire detection algorithms.

5.3 Gas Flares

One unintended but important application of FILDA involves the detection of gas flares. While other algorithms exist for the sole purpose of flare detection and characterization using other satellite platforms (e.g. Muirhead and Cracknell, 1984; Anejionu et al., 2015) or use fundamentally different parts of the infrared spectrum (as in Elvidge et al., 2013), FILDA shows potential with nocturnal gas flaring detection based on the reduction of the BT_4 threshold. Two gas-flaring regions are examined; first, the Khanty-Mansiysk region of Russia is examined because of its rapid development in recent years and its high volume of flared gas. Second, offshore flares in the Niger Delta are investigated in order to test FILDA's potential for monitoring flares over open water.

Although gas flares do not pose a direct risk to life and property, they do emit hazardous compounds as by-products of incomplete combustion. These include soot, partially-combusted hydrocarbons, CO, CO_2, NO_x, and SO_2 (Ismail and Umukoro, 2012). Unfortunately, it is often difficult to obtain flare volume and location information from their operators due security concerns and lack of accountability, especially in poorer countries (Anejionu et al., 2015). Remote sensing fills that important void in the estimation of gas

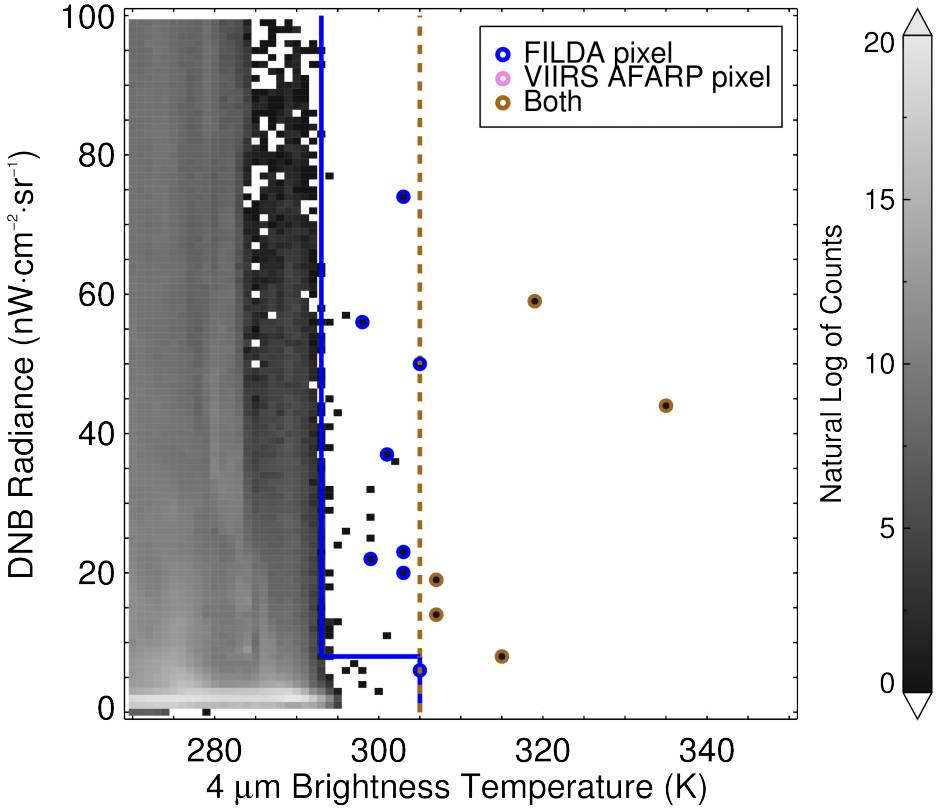

Figure 5.9: Two-dimensional histogram of the granule used in Figure 5.8 showing fire pixel classifications for both FILDA and AFARP. As in Figure 5.5, blue circles indicate FILDA fire pixels, while the pink circles are AFARP detections. The solid blue line represents FILDA's thresholds, while the gold dashed line is the 305 K 4 µm BT potential fire pixel threshold used by AFARP (and FILDA with little light). It should be noted that this scatter plot includes the entire granule and not just the region shown in the previous figure.

flaring emission impacts.

Khanty-Mansiysk is an oil boom town is located in Central Russia; in 2011, it constituted over half—51.3%—of Russia's oil production and continues to increase (newsru.com, 2012). A very small portion of the region is displayed in Figure 5.10. Figure 5.10(a) shows a portion of the flare complex located near the Ob River; notice that in the center of the image, there is a FILDA detection over what is seemingly wilderness. Interestingly, this is an artifact of the region's rapid growth—further enlargement yields an expanding oil extraction complex

whose image was taken too recently to be integrated into Google's zoomed-out map mosaic. The flare signatures are two flow stations, which are structures that collect natural gas from smaller wells and flare them in a centralized location. In figure 5.10, the flare signature is visible in all bands, though the DNB highlights the feature exceptionally well. Unfortunately, the BT_4 threshold in AFARP is too high to consider them as potential fire pixels.

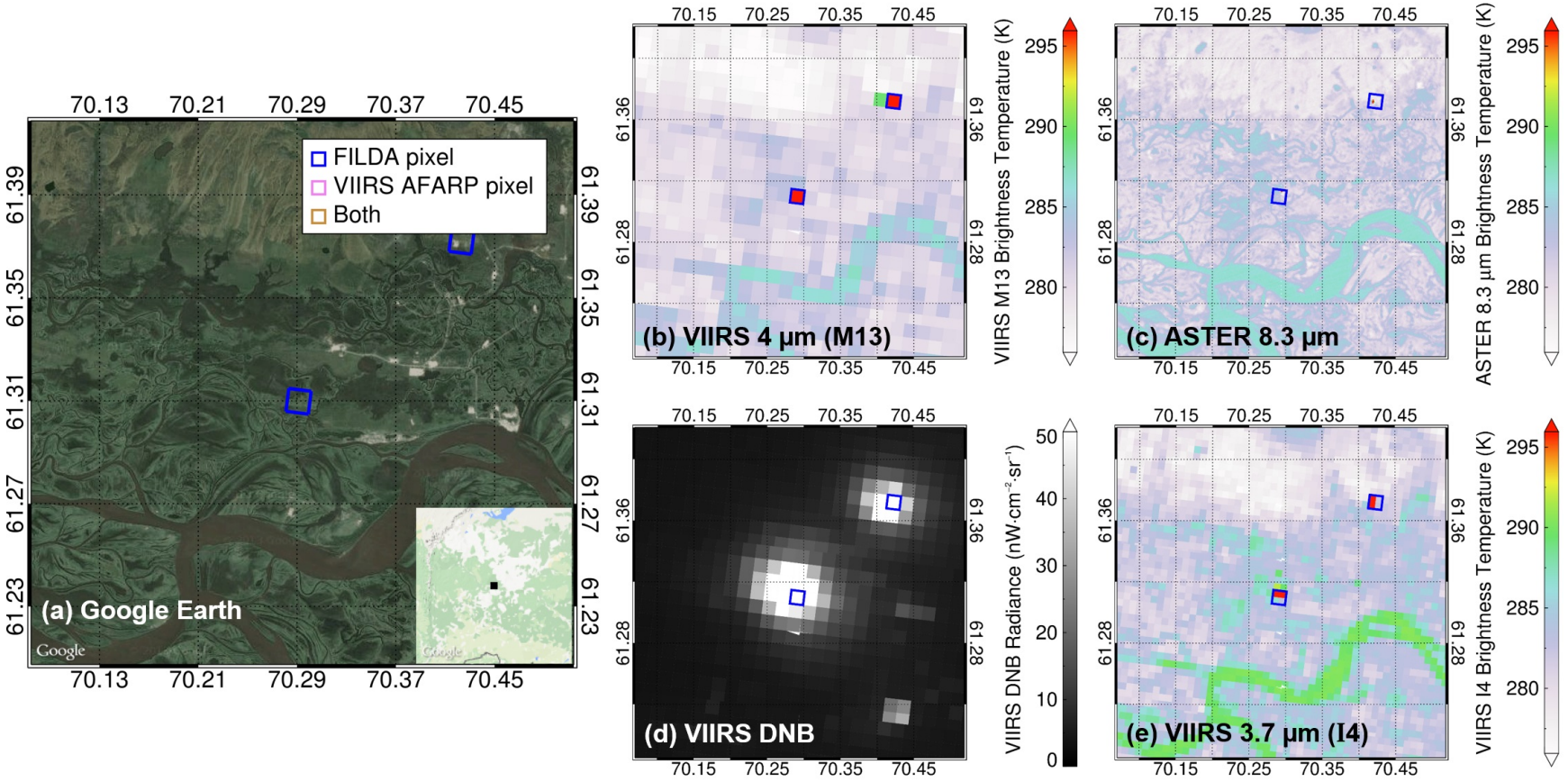

Figure 5.10: Multi-band/sensor view of two gas flares in the Khanti-Mansiysk region of Russia from 20:52 UTC (2:52 AM local time) on 9 August 2013 by VIIRS. ASTER [panel (c)] scanned the flares at 16:44 UTC (10:44 PM local time). The blue boxes are pixels detected by FILDA (AFARP omitted both flares). The BT_4 threshold is 287 K, and the DNB threshold is 6 $nW/cm^2 - sr$.

The Niger Delta, like the Khanty-Mansi region, is also home to large-scale oil and gas production. The region is infamous for the ecological devastation that petroleum extraction has wreaked on its fragile estuarial ecosystems (Bayode et al., 2011) which include large mangroves. Nigeria has historically been one of the worst offenders by flaring 99% of its natural gas production as recently as 2003 (The Ministry of Environment of the Federal Republic of Nigeria, 2003), but laws passed in recent years banning the practice have reduced the portion of gas flared to under 20% (World Bank, 2014). Because of the inherent security risks from civil unrest in the region, field studies are rarely conducted, and most flaring estimates are derived from satellite data, such as in Anejionu et al. (2015).

While both AFARP and FILDA are able to identify large flow stations on land (more so with FILDA), offshore oil rig flares are not identified by AFARP because all water pixels are initially screened out by the algorithm. As mentioned before, the purpose for the filtering is mainly due to daytime considerations; sun glint often creates false positives. With the inclusion of water pixels, offshore rigs are easily identified. Using the VIIRS scene from 01:20:47 UTC on 19 December 2013 which is looking over parts of the Niger Delta and Southern Atlantic, flares stand out from the background with both the DNB and M13. Table 5.1 shows the detections of the granule and their associated information. Of particular note is that most of these offshore flares listed in the table are extremely hot and bright—even well above the minimum detection threshold for AFARP. Figure 5.11 shows some of these flare detections, with hot spots apparent in every band. Unfortunately, many of the smaller flares in the image are not detected. Some flares are omitted because their BT_4 signatures are masked by overlying marine stratus clouds, despite their visible DNB signatures. Similarly, other flares are omitted because they are smaller and their ΔBT signatures are less than 10 K. The I4 band does, however, highlight many of these smaller hot spots; this feature might be useful to include in future refinements, as it is colocated with the M-bands. Despite missing these smaller flares, FILDA detects larger flares and—unlike AFARP—works well

Table 5.1: Offshore flare characteristics from the 01:20:47 UTC 19 December 2013 VIIRS granule as detected by FILDA. The BT_4 threshold is 297 K, and the DNB threshold is 20 nW·cm^{-2}·sr^{-1}.

BT_4 (K)	BT_{11} (K)	DNB (nW·cm^{-2}·sr^{-1})	Longitude (°)	Latitude (°)
311.52	297.38	6256.58	4.58	5.38
318.90	297.63	1378.44	4.34	5.35
325.39	291.12	5911.93	7.78	4.24
348.84	294.31	3455.12	7.79	4.23
317.51	294.95	3988.30	8.09	4.12
317.76	295.08	4437.07	7.51	4.13
306.04	294.78	2191.45	7.52	4.13
304.37	293.71	1432.80	4.61	4.55
305.89	295.21	3523.28	7.28	3.99
323.75	295.82	10294.53	7.29	3.98
308.99	294.92	5426.80	8.10	3.85
331.31	296.45	9777.56	7.39	3.57
311.29	293.35	4372.14	9.23	1.40
303.87	288.29	164.84	9.94	-1.52

over open water.

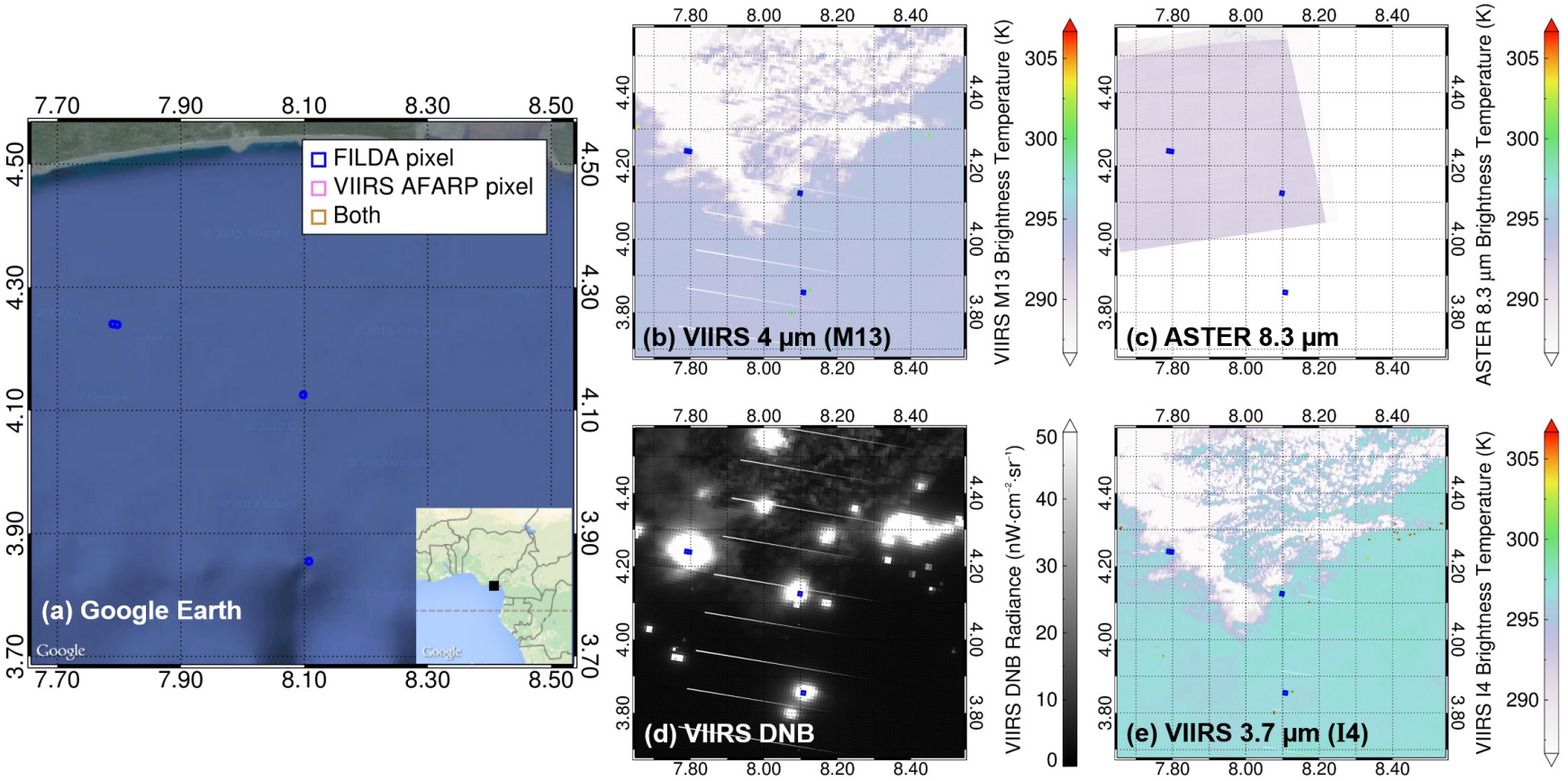

Figure 5.11: Multi-band/sensor views of offshore gas flares by VIIRS and ASTER, using the same 01:20:47 UTC 19 December 2013 VIIRS granule as in Table 5.1. Larger flares are identified by FILDA, but smaller flares are still omitted. The ASTER overpass time was 21:55:58 UTC on 18 December 2013.

Chapter 6

Conclusion

This paper presents a novel approach to detect wildfires, biomass burning, and gas flares at night by incorporating visible light into the fire detection algorithm. Although Croft proposed the idea over 40 years ago, the fire algorithms developed since then only utilize the infrared portion of the electromagnetic spectrum. Owing to the launch of VIIRS in October of 2011 with its day-night band, we are finally able to incorporate visible data into these algorithms and further refine them. The *FI*re*L*ight *D*etection *A*lgorithm (FILDA) is the result of this approach. Based on the official VIIRS fire product algorithm known as the Active Fire Application Related Product (AFARP), it incorporates DNB radiances as well as IR signatures.

Many case studies (including those not presented here) show that FILDA has potential in improving the detection of wildfires. Overall, the number of FILDA detections nearly double that of AFARP. This mainly occurs at the fringes of fire fronts and semi-smoldering and scorched terrain left in their wake where the BT_4 were slightly under AFARP detection thresholds. In addition to wildfires, FILDA improves the detection of gas flares. While significant numbers of small flares are still omitted by FILDA because of their weak IR signature, many more flow stations are observed than in AFARP. The biggest improvement,

however, is with the detection of offshore oil rig flares, since FILDA does not screen out water pixels from the selection of potential fire pixels. While FILDA is unable to identify the majority of smoldering fires due to the lack of emitted light, they would be omitted by AFARP regardless.

Of particular note is the power FILDA has for detecting smaller and cooler fires that would otherwise be omitted from detection by AFARP. The Rim Fire in California is a good example of this; FILDA is able to identify the fire the first night it burned, while AFARP required an additional day for the Rim Fire pixels to reach detection thresholds. This has broad implications for the fire response and management community, since earlier response is paramount to controlling fires while they are still manageable. This is further enhanced because winds and ambient temperatures usually decrease with the onset of darkness. If this approach is utilized, it could help reduce property damage and loss of life.

Appendix A

First Global Analysis of Saturation Artifacts in the VIIRS Infrared Channels and the Effects of Sample Aggregation

A.1 Introduction

On 28 October 2011, the Suomi National Polar-orbiting Partnership (S-NPP) satellite was launched from the Vandenberg Air Force Base in California, and now orbits with a mean altitude of 840 km above the Earth in sun-synchronous orbit. Located aboard S-NPP, the Visible Infrared Imaging Radiometer Suite (VIIRS) is a 22-band scanning radiometer with a nominal spatial resolution of 375 m in the five imagery bands (I bands) and 750 m in both the 16 moderate resolution bands (M-bands) and the Day-Night-Band (DNB) (Cao et al., 2014; Csiszar et al., 2013; Wolfe et al., 2013; Schroeder et al., 2014). The sensor data records (SDR) of calibrated radiances and brightness temperatures cover a spectral range

from 0.411 μm to 11.87 μm and are used in a wide range of Earth observation applications including fire detection and characterization, retrieval of cloud and aerosol properties, and land and sea surface temperature estimation (Hillger et al., 2013). The VIIRS sensor was designed to improve upon legacy instruments, such as the MODerate Resolution Imaging Spectroradiometer (MODIS), Advanced Very High Resolution Radiometer (AVHRR), and Operational Line Scanner (OLS). One significant enhancement relative to these legacy sensors is that VIIRS does not experience the significant off-nadir pixel growth affecting sensors like MODIS; VIIRS pixels at the scan edge are only two to four times the size of nadir pixels, while MODIS exhibits a growth factor of ten, for example (Wolfe et al., 2013). For the M-bands, VIIRS delivers SDRs of calibrated radiances and brightness temperatures with a pixel instantaneous field of view (IFOV) of 0.75 × 0.79 km at nadir, which increases to 1.66 × 1.71 km at the edge of the scan (Cao et al., 2014), while the five imagery bands have smaller IFOVs ranging from 0.38 × 0.39 km to 0.83 × 0.86 km at the scan edge.

The spatial resolution of VIIRS is preserved across the scan by employing asymmetrical detectors in conjunction with a unique sample aggregation scheme, as illustrated by Figure A.1, which combines multiple samples from one rectangular detector into single raw data record (RDR) pixels consisting of digital counts. This processing is done onboard the satellite, except for the dual-gain bands whose aggregation is done on the ground (Wolfe et al., 2013). As a result, the RDR has three aggregation zones. The 3:1 aggregation zone refers to scan angles between 0° (nadir) and 31.72°, where the value of each pixel is actually the average of three individual samples. Similarly, in the 2:1 aggregation zone (scanning angles between 31.72° and 44.86°), two samples from the same detector are aggregated to form a pixel. No sample aggregation is performed in the 1:1 aggregation zone (scan angles greater than 44.86°); thus, each pixel is calculated from a single detector sample. Once the RDR has been generated, it is later processed into a calibrated SDR, retaining the characteristics from aggregation.

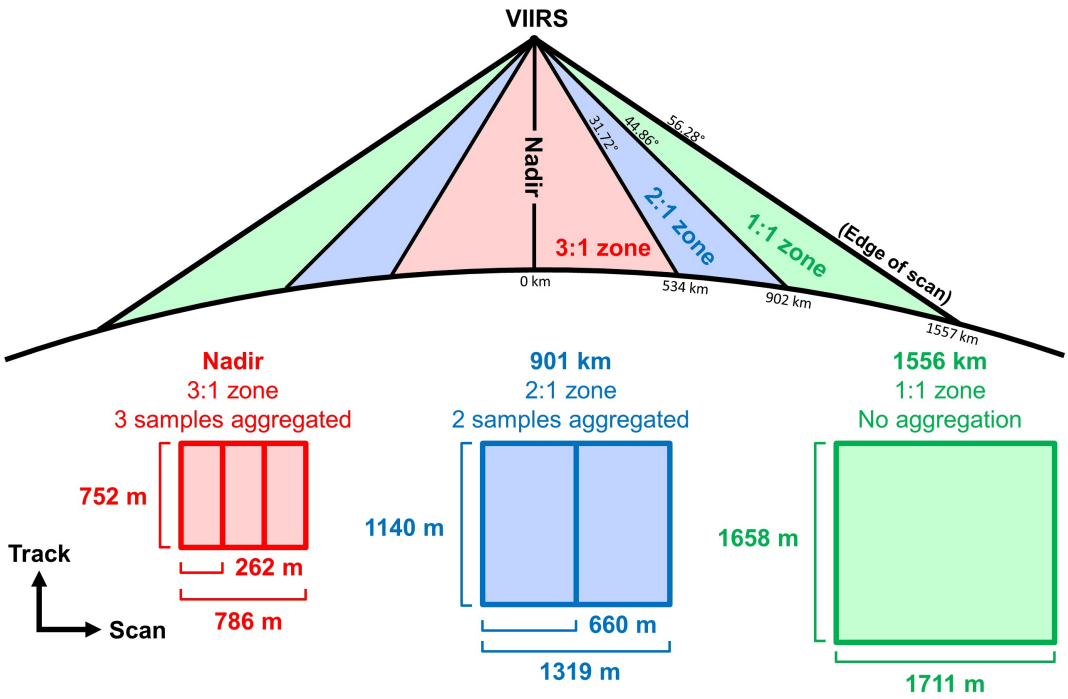

Figure A.1: VIIRS aggregation scheme (not to scale) and sample dimensions over the equator with an orbital altitude of 830 km (Wolfe et al., 2013). The individual rectangles represent samples from an M-band detector, shaded by aggregation zone.

While the VIIRS aggregation scheme effectively reduces pixel footprint growth across the scan, it also results in fundamental differences in the data characteristics among the three aggregation zones, especially when detector saturation occurs. The VIIRS on-board electronics module does not flag the data if an individual sample saturates before aggregation occurs. Consequently, the aggregation of samples does not account for saturation effects, which may result in biases or artifacts for pixels containing active biomass burning or other heat sources that have the potential to cause detector saturation. In the case when an individual sample is saturated and then aggregated with unsaturated samples, the resulting pixel will have a radiance bias associated with saturation, even if the reported pixel radiance is well below the detector saturation limit. This study investigates the frequency and effects

of saturated samples in the VIIRS infrared (IR) channels, and evaluates the potential for biases and artifacts in the VIIRS SDR caused by onboard sample aggregation. This study represents a first attempt to: (a) derive an empirical method for identifying possible partial saturation and (b) determine thresholds to filter partially or fully saturated pixels in bands that are relevant to the detection and characterization of hot targets.

A.2 Data Set Description

In order to facilitate the analysis of saturation potential in VIIRS data, a NOAA Joint Polar Satellite System (JPSS) Proving Ground product named Nightfire is used in this study (Elvidge et al., 2013). Nightfire is utilized because it contains an extensive set of pre-screened hot pixels, allowing for fast analysis of months of data. The Nightfire algorithm selects thermally anomalous pixels detected in the VIIRS shortwave infrared (SWIR) 1.6 μm band (M10) (Elvidge et al., 2013), rather than utilize the 4 μm range that is traditionally used for fire detection (Peterson et al., 2013). VIIRS is unusual in that it records some near-infrared (NIR) and SWIR data during nighttime (bands M7, M8, and M10, Table A.1), which allows for easy and rigorous detection of hot sources due to the lack of background (solar) radiation. The nighttime background radiance at 1.6 μm is very low, generally of the same order of magnitude as dark current noise in the sensor. M10 is therefore selected as the primary band of Nightfire to detect thermally radiant objects, especially gas flares with burning temperatures up to 1800 K (Elvidge et al., 2013). During nighttime, pixels more radiant than the background DC (digital count) plus four standard deviations of DC are first flagged as thermally anomalous candidate pixels. The background DC is the mean DC of all non-hot pixels (DC value ≤ 100) contained in each aggregation zone for one VIIRS granule, and the standard deviation is calculated using the same criteria. To filter the noise in M10 caused by high-energy particles that frequently hit the sensor within the South Atlantic

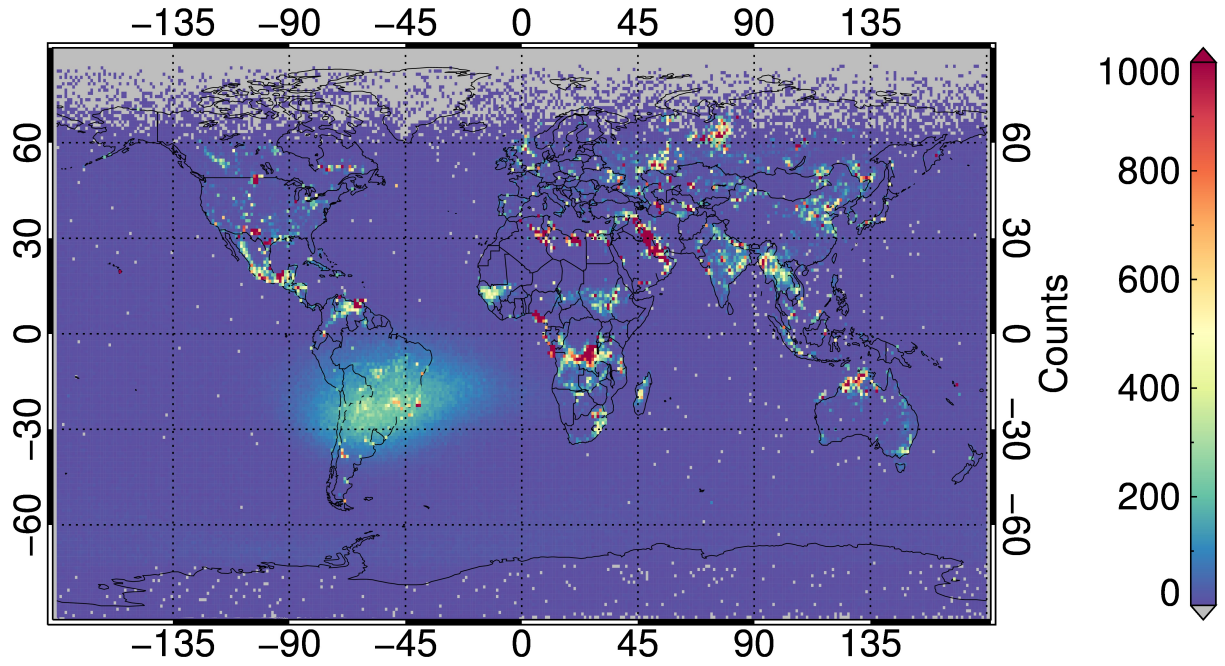

Figure A.2: Global distribution of M12 counts in the Nightfire data set, gridded to 1°×1°. Clustering of counts can be observed in regions of frequent biomass burning and gas flaring. Despite Nightfires attempts to filter it out, the blue region on and around South America still manifests as the South Atlantic Anomaly (SAA), similar to what has been observed from other sensors observing near the 1.6 μm range (Casadio and Arino, 2011).

Anomaly (SAA) (Casadio and Arino, 2011; Schroeder et al., 2014) and auroral areas, the Nightfire algorithm conducts a second check on the hot pixel detected by M10 with other NIR/SWIR bands (M7 and M8) using the same technique as for M10. Lastly, the algorithm attempts to fit a Planck curve to the retrieved radiances to obtain the temperature and area of the emitting source using the Simplex Optimization Method (Lagarias et al., 1998). A more thorough discussion of the Nightfire algorithm can be viewed in Elvidge et al. (2013).

While Nightfire provides atmospheric-corrected data, only the uncorrected calibrated radiances for the nine M-bands (Table A.1) for each pixel are examined in this study. Atmospherically-corrected data and retrieved hot spot properties are not investigated. Statistical examination of the Nightfire data (Table A.1) indicate a discontinuity between data

Table A.1: Spectral characteristics and statistics of observed radiance for each VIIRS band (Cao et al., 2014) in the Nightfire data set.

Band	Spectral Range (μm)	Central λ (μm)	Specification Max[1]	Obs. Max[1]	Above Spec. Fraction[2] (%)	Obs. Fraction[3] (%)
M7	0.843 - 0.881	0.86	349	24.2	0	N/A
M8	1.225 - 1.252	1.24	165	80.3	0	N/A
M10	1.571 - 1.629	1.60	71.2	75.0	0	N/A
M12	3.598 - 3.791	3.69	353	359	0.22	0.15
M13[4]	3.987 - 4.145	4.06	634	533	0	N/A
M14	8.407 - 8.748	8.58	336	349	0.002	0.0005
M15	10.234 - 11.248	10.74	343	359	0.001	0.0003
M16	11.405 - 12.322	11.86	340	356	0.001	0.0003
DNB[5]	0.5 - 0.9	0.70	0.0186	N/A	N/A	N/A

[1]Unit is $W{\cdot}m^{-2}{\cdot}sr^{-1} \cdot \mu m^{-1}$ for M7, M8, M10; K for M12-M16; $W{\cdot}cm^{-2}{\cdot}sr^{-1}$ for the DNB.
[2]Percentage of pixels above 99.9% of the design specification maximum from (Cao et al., 2014).
[3]Percentage of pixels above 99.9% of the observed maximum.
[4]Primary VIIRS fire detection band.
[5]The DNB has a very broad spectral range (Liao et al., 2013) and was not analyzed for saturation.

before and after 17 March 2013. Therefore, the earlier data are excluded, leaving Nightfire data from 18 March 2013 to 14 July 2013 available for use in this study. After screening out records with missing data (less than 0.01% of the data), this time period yields 1,861,865 thermally anomalous pixels. The geographic distribution of the filtered Nightfire data is shown in Figure A.2, highlighting regions of frequent biomass burning (Central Africa, Central America, Southeast Asia), as well as regions that commonly flare gas, such as the Persian Gulf, North Dakota, and Nigeria.

A.3 Analysis and Results

The analysis is divided into three parts. First, the nine M-bands from Table A.1 are scrutinized by constructing histograms to identify which bands are fully saturating. Full saturation

would be manifested by sudden or unexpected peaks in frequency at the highest radiance bin. Second, the most-frequently saturating band's data are separated by aggregation mode to determine if there is a relationship with sample saturation and aggregation scheme. In this case, scatterplots of the data between saturating and a non-saturating band are constructed to look for distinct populations of pixels unique to each mode. The third and final step of the analysis attempts to verify the relationship between sample saturation and aggregation by statistically simulating the effects of partial saturation. This is accomplished by using the properties of the un-aggregated data (from the 1:1 aggregation zone) to generate synthetic populations of detector data that can be aggregated to match the VIIRS sample aggregation scheme, and comparing the resulting histograms of the synthetic data to the observed distributions of each aggregation mode.

A.3.1 Band-by-band Detection of Saturation

From the radiance histograms of each band (Figure A.3), significant saturation is observed in the 3.69 μm (M12) band, which is highlighted by the sudden density peak at 3.39 $W{\cdot}m^{-2}{\cdot}sr^{-1} \cdot \mu m^{-1}$, representing 0.15% of the data (red arrow). The approximate radiances corresponding to the theoretical limits described by (Cao et al., 2014) are indicated by the vertical dashed red lines in Figure A.3. The maximum observed radiance is slightly higher than the theoretical maximum; 3.39 $W{\cdot}m^{-2}{\cdot}sr^{-1} \cdot \mu m^{-1}$ has a corresponding brightness temperature of ∼359 K at the center wavelength of 3.69 μm in comparison to the 353 K brightness temperature limit reported by (Cao et al., 2014). The incidence of partial pixel saturation as a possible side-effect of aggregation is noted near 1.3, 1.8, and 2.3 $W{\cdot}m^{-2}{\cdot}sr^{-1} \cdot \mu m^{-1}$, which can be seen by the slight and smoothed peaks near those radiance values. Figure A.4 shows the global distribution of fully saturated (3.39 $W{\cdot}m^{-2}{\cdot}sr^{-1} \cdot \mu m^{-1}$) M12 pixels aggregated to a $1^\circ \times 1^\circ$ grid; many of the same regions with hotspots in Figure

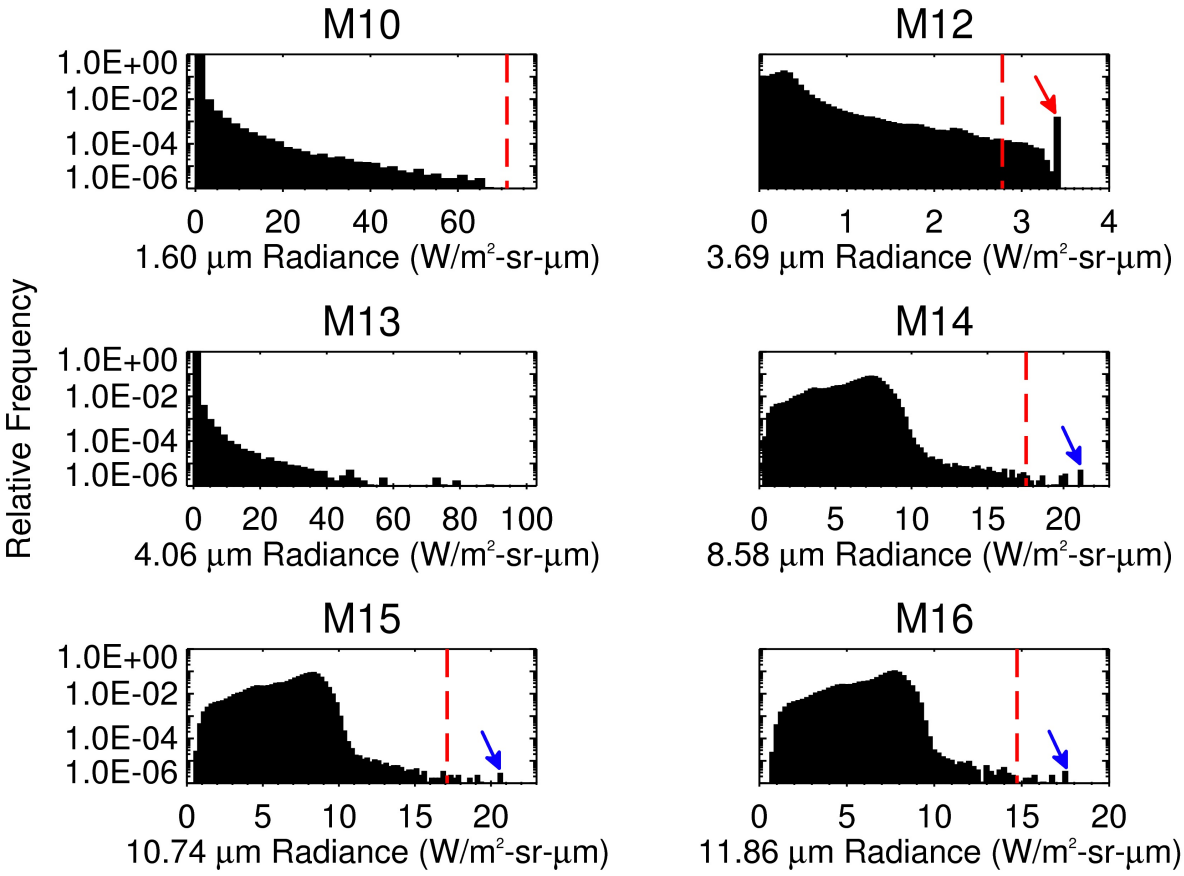

Figure A.3: Analysis of the infrared channels contained in Nightfire. The published saturation limits for each band are shown by the red dashed lines (except M13, much higher than observed data). The only channel exhibiting easily-discernible saturation is M12, which has been marked with a red arrow. Blue arrows mark possible saturation features in M14, M15, and M16.

A.2 are visible, but the SAA is notably absent.

Clustering of values near the maximum observed bins from Figure A.3 gives qualitative evidence of possible saturation in the M14, M15, and M16 bands (marked by the blue arrows). However, for bands other than M12, the percentage of pixels that lie above 99.9% of the nominal saturation levels and observed maximum values is very low (e.g. less than 0.002%, Table A.1, right columns), suggesting that saturation effects in nocturnal scenes are very rare in these bands. Bands M10 and M13 do not experience saturation in this data set.

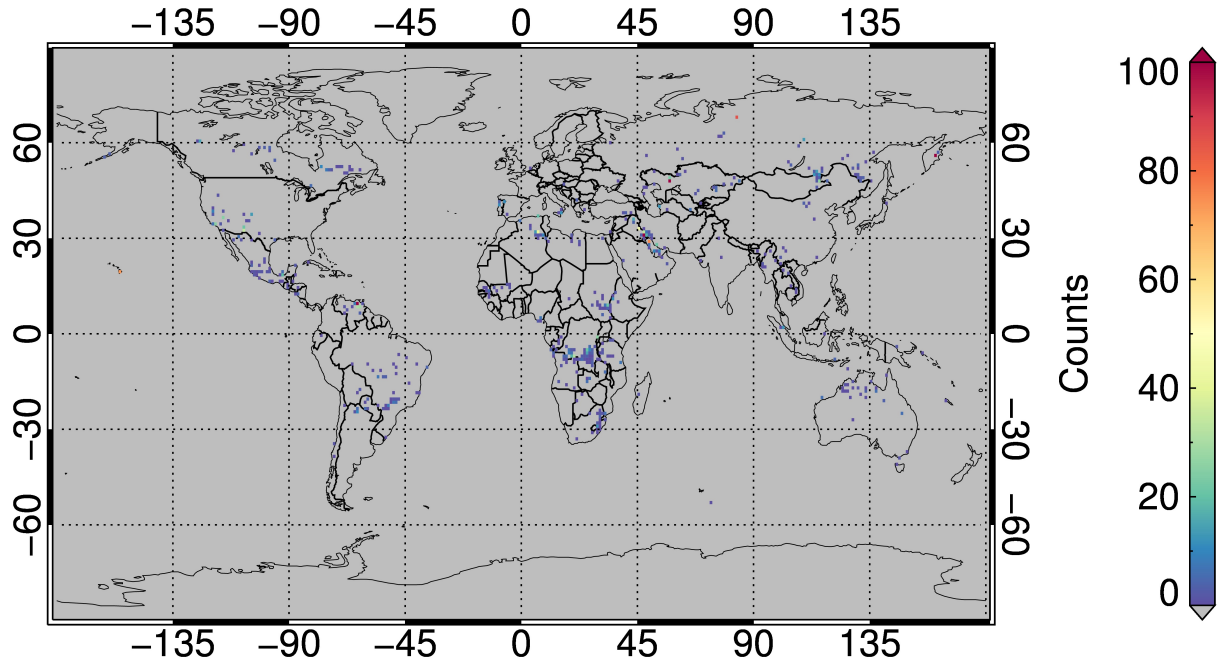

Figure A.4: Global distribution of Nightfire detections at the M12 saturation limit (3.39 $W{\cdot}m^{-2}{\cdot}sr^{-1} \cdot \mu m^{-1}$), aggregated to a 1°×1° grid. Note that the color scale is an order of magnitude lower than Figure A.2.

A.3.2 M12 Saturation Aggregation Zone Dependence

In order to determine the effects of sample saturation in the M12 band, the data is segregated according to aggregation zone. Scatterplots of 3.69 μm/4.06 μm (M12/M13) ratio vs. 4.06 μm (M13) for each aggregation zone are shown in Figure A.5. The ratio of M12/M13 is used for comparison since M13 does not saturate and lies in close spectral proximity to M12. The three panels illustrate the 1:1, 2:1, and 3:1 aggregation zones, respectively. The 1:1 pixels (green dots, Figure A.5a) show the baseline pattern for M12, where the ratio of M12/M13 varies up to the detector saturation point of 3.39 $W{\cdot}m^{-2}{\cdot}sr^{-1} \cdot \mu m^{-1}$. For M13 radiances above this limit, M12/M13 is truncated, indicating that M12 is saturating while M13 is not (labeled 1 in Figure A.5a). The variability of M12/M13 at low M13 radiances shows a spread of ratios due to different thermal properties, owing to the atmospheric effects and the

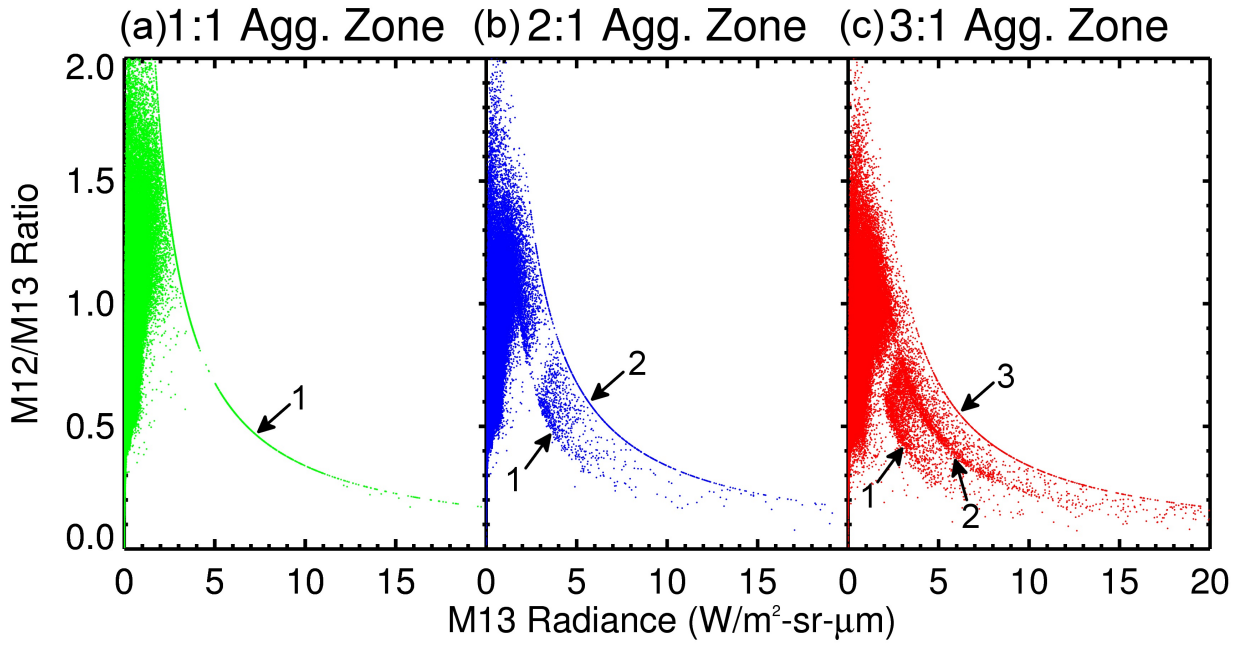

Figure A.5: Ratio of M12/M13 radiance versus M13 radiance separated by scanning angle to show the effects of on-board aggregation. (left) 1:1 aggregation zone points (44.86°+); (center) 2:1 aggregation zone points (31.72°-44.86°); (right) 3:1 aggregation zone points (0°-31.72°). Aggregation results in concentrations of values along curves at lower ratios than the detector saturation limit depending on how many samples are aggregated into one pixel. These curves are overlaid with the number of samples saturating for each population.

Planck function's sensitivity to temperature for differing wavelengths. Despite this, as the M13 radiance increases, the M12/M13 ratio converges to a curve determined by the M12 saturation limit.

The 2:1 aggregation zone (Figure A.5b) shows a similar pattern with one important and noticeable difference. As the M13 radiance increases, the M12/M13 ratio converges to two clusters with a spread of points between them. The lower cluster (labeled 1) reflects the case when one sample saturates while the other aggregated sample does not. As the ratio

increases for the same M13 radiance value, there is still one saturated M12 sample, but the neighboring aggregated M12 sample is reporting increased radiances until both samples saturate (labeled 2). That is visible as the detector saturation limit of the M12/M13 ratio with the same M12 radiance of 3.39 $W \cdot m^{-2} \cdot sr^{-1} \cdot \mu m^{-1}$.

Lastly, in the case of the 3:1 aggregation scheme (Figure A.5c), there are three populations of curves, owing to the three samples that are averaged together. The lowest cluster represents the case when one of the aggregated M12 samples saturates (labeled 1), but the two other samples do not. The middle ratio population for a given M13 radiance is for a situation where two samples saturate, but the third does not (labeled 2). Finally, the uppermost population is where all three aggregated M12 samples saturate (labeled 3).

A.3.3 Diagnosing and Verifying New Saturation Thresholds

To confirm that these features are consistent with aggregation effects, a statistical method was devised to simulate the observed distribution of radiances in each aggregation zone. 30 million values are randomly drawn from the observed M12 1:1 aggregation zone. The 2:1 aggregation zone is simulated by drawing 15 million random pairs from the 1:1 aggregation zone and averaging each pair, while the 3:1 aggregation zone is simulated by drawing 10 million triplets from the 1:1 aggregation zone and averaging them. The results of these simulations are displayed in Figure A.6, which is divided into nine panels. In each panel, the colored bars show the observed distribution from the Nightfire data and the black lines show the statistically created distributions. The three rows represent the aggregation zones starting with 1:1 at the top and ending with 3:1 at the bottom, while the three columns are 3.69 μm radiance (M12), 4.06 μm radiance (M13), and 3.69/4.06 μm ratios (M12/M13), respectively from left to right. The statistically simulated radiance values almost exactly reproduce the observed distributions of radiances from the 1:1 aggregation zone (top row of

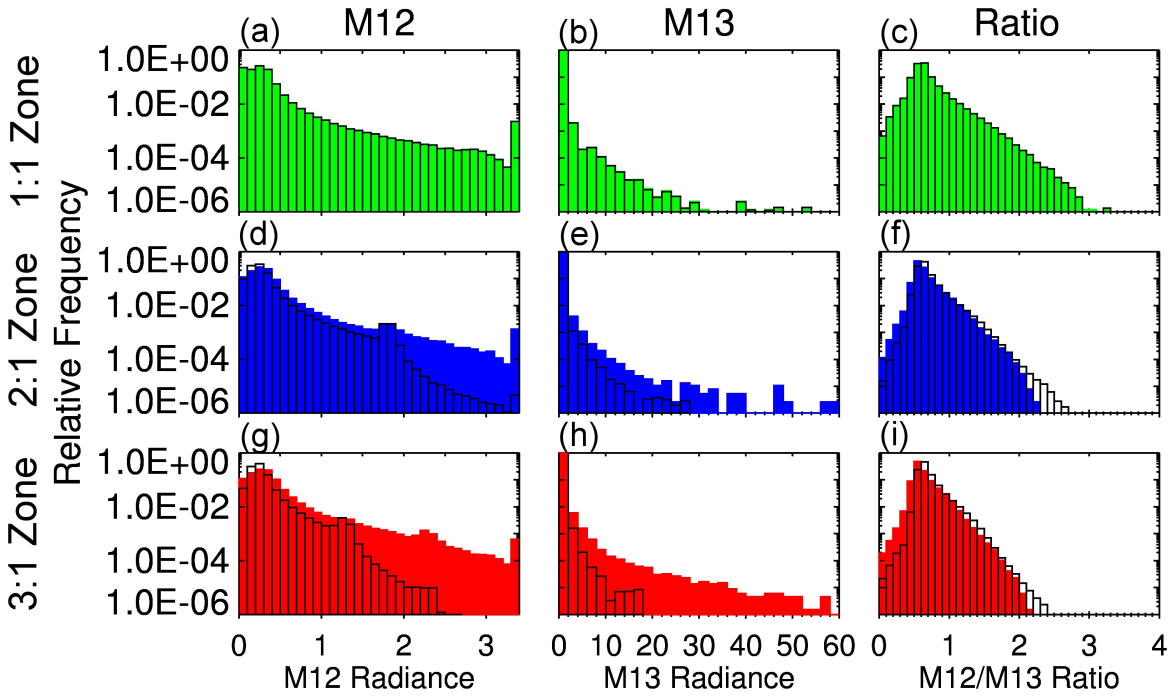

Figure A.6: Distribution of radiances observed (filled bars) and synthetically calculated (black outlines) for each aggregation zone. The three rows represent the different aggregation modes starting with 1:1 at the top and ending with 3:1 at the bottom, while the three columns are M12 radiance, M13 radiance, and M12/M13 ratios, from left to right. Solid bars represent the observed distributions of radiances, and the black outlines represent the synthetic distributions made by averaging samples drawn from the edge-scan data set (see section III-C for details).

Figure A.6). The randomly selected pairs and triplets (second and third rows of Figure A.5) show peaks of density in the same locations as the observed data, indicating the effects of saturation well below the detector saturation limit.

Saturation can be seen to affect radiances as low as 1.7 $W{\cdot}m^{-2}{\cdot}sr^{-1}{\cdot}\mu m^{-1}$ (~337 K at 3.69 μm) for the 2:1 aggregation zone (Figure A.6d). In the 3:1 aggregation zone, the influence of an individual saturated sample becomes apparent at radiances of just 1.3 $W{\cdot}m^{-2}{\cdot}sr^{-1}$ ·

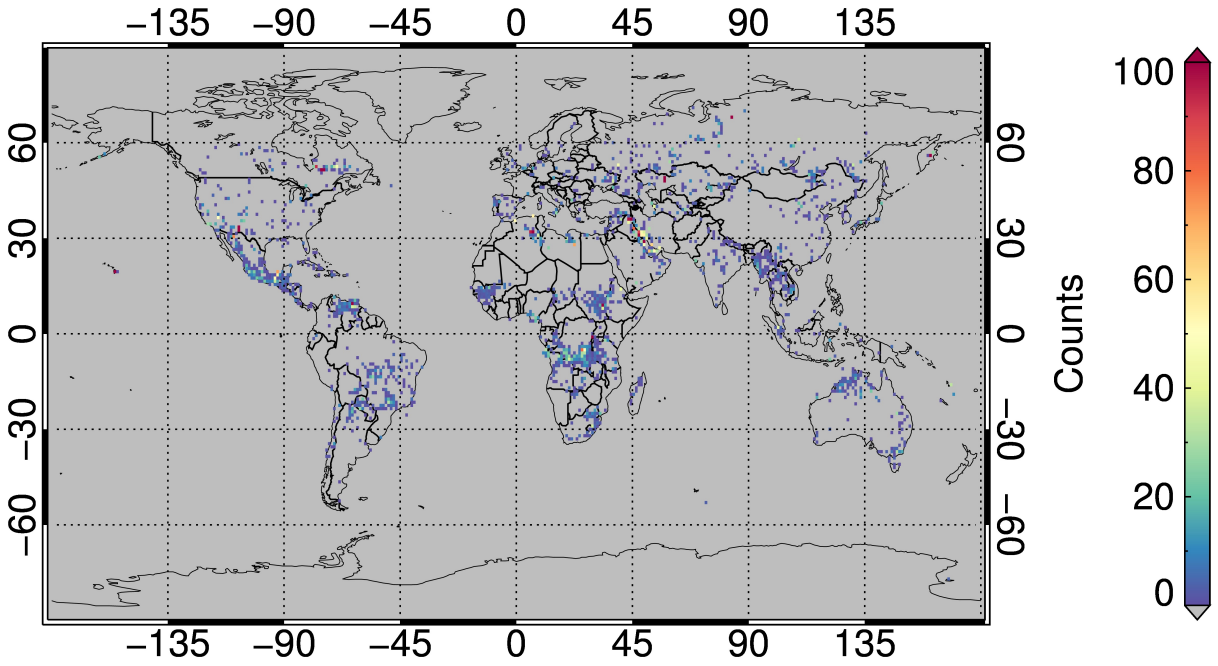

Figure A.7: Global distribution of the partially-saturated M12 pixel counts to a 1°×1° grid. Partial saturation is determined by taking lowest temperature at which saturation artifacts are observed in each aggregation zone. The color scale is the same as Figure A.4.

μm^{-1} (∼330 K). The second column shows the observed and synthetic distributions for the M13 (4.06 μm) band, where no unusual peaks in density are noted. The far right column shows suppression of high values of M12/M13 with aggregation, consistent with the effects of averaging. The geographic distribution of potential partially saturated pixels is displayed in Figure A.7, where data are mapped only if the radiance values reach above the thresholds of possible partial saturation (1.3 $W \cdot m^{-2} \cdot sr^{-1} \cdot \mu m^{-1}$ for 3:1 aggregation, 1.7 $W \cdot m^{-2} \cdot sr^{-1} \cdot \mu m^{-1}$ for 2:1 aggregation, and 3.39 $W \cdot m^{-2} \cdot sr^{-1} \cdot \mu m^{-1}$ for 1:1 aggregation). In comparison to the observed detector saturation limit (Figure A.4), a much larger area is impacted by partial saturation.

While the general pattern of the observed and simulated distributions is similar, especially the features caused by detector saturation, large discrepancies exist. One main difference

stems from sample correlation. Normally, when VIIRS scans a scene, adjacent samples will observe a similar environment; that is, if one sample scans a fire, the chances are high that the adjacent samples(s) will also scan hot terrain. This greatly increases the frequency of high temperatures occurring in the observations compared with randomly selected samples. Another compounding factor is the difference in IFOV, which is dependent on scan angle. While the pixel footprint change is reduced by aggregation, detector footprint sizes for VIIRS still increase significantly with scan angle. Thus, the detector IFOV near nadir is much smaller than at the scan edge, which leads to higher fire fractions and, subsequently, increased occurrence of very high radiances in the near-nadir samples when compared with the 1:1 aggregation zone samples. These two effects have similar impacts on the observed distribution; therefore, they cannot be easily separated for analysis or considered in the simulated distributions. This demonstrates that extrapolation from the 1:1 zone tends to underestimate the occurrence of saturation in the 2:1 and 3:1 aggregation regimes.

A.4 Summary and Conclusions

This study investigated the prevalence and influence of detector saturation when the VIIRS sample aggregation scheme is applied. It should be noted that saturation may occur more frequently than the Nightfire data set indicates because fires tend to burn hotter in the daytime than at night. The only band to suffer from significant deleterious detector saturation is the 3.69 μm band (M12), but there is some evidence to support saturation in the other single-gain TIR channels that might be more apparent in a larger data set. The maximum radiance values recorded by VIIRS in those bands are significantly higher than the published maxima in (Cao et al., 2014). For the M12 band, distinct clustering of pixel radiances below the detector saturation limit of 3.39 $W \cdot m^{-2} \cdot sr^{-1} \cdot \mu m^{-1}$ (∼359 K) appear in the data from the 2:1 and 3:1 aggregation zones. The 1:1 aggregation zone's saturation limit

is thus 3.39 $W{\cdot}m^{-2}{\cdot}sr^{-1} \cdot \mu m^{-1}$ (∼359 K), while the 2:1 aggregation zone exhibits saturation at 1.7 $W{\cdot}m^{-2}{\cdot}sr^{-1} \cdot \mu m^{-1}$ (∼337 K), and the 3:1 aggregation zone is susceptible to saturation at only at 1.3 $W{\cdot}m^{-2}{\cdot}sr^{-1} \cdot \mu m^{-1}$ (∼330 K).

VIIRS does not record when saturation occurs in individual samples. Therefore, it is impossible to know if a pixel is affected by saturation in the M12 band beyond its respective saturation threshold. The potential for biases in pixel radiance due to unidentified saturation is a significant problem for quantitative use of the M12 band for applications that use hot pixels, such as for multispectral fire property retrievals. M12's intended use for sea surface temperature derivation (Lee et al., 2006), (Cao et al., 2014) should not be impacted, provided pixels are filtered to avoid hot sources such as gas flaring. For applications that require quantitative evaluation of hot sources, the aggregation scheme determines the upper limit of radiances known to be unsaturated.

Bibliography

V. G. Ambrosia, S. W. Buechel, J. A. Brass, J. R. Peterson, R. H. Davies, R. J. Kane, and S. Spain. An integration of remote sensing, gis, and information distribution for wildfire detection and management. *Photogrammetric Engineering and Remote Sensing*, 64(10): 977–985, OCT 1998.

O. C. D. Anejionu, G. A. Blackburn, and J. D. Whyatt. Detecting gas flares and estimating flaring volumes at individual flow stations using modis data. *Remote Sensing of Environment*, 158:81–94, MAR 2015. doi: 10.1016/j.rse.2014.11.018.

O. Arino and J. M. Melinotte. The 1993 africa fire map. *International Journal of Remote Sensing*, 19(11):2019–2023, JUL 20 1998 1998. doi: 10.1080/014311698214839.

O. J. A. Bayode, E. A. Adewunmi, and S. Odunwole. Environmental implications of oil exploration and exploitation in the coastal region of ondo state, nigeria: A regional planning appraisal. *Journal of Geography and Regional Planning*, Vol. 4 No. 3:110–121, MAR 2011.

C. Cao, F. J. D. Luccia, X. Xiong, R. Wolfe, and F. Weng. Early on-orbit performance of the visible infrared imaging radiometer suite onboard the suomi national polar-orbiting partnership (s-npp) satellite. *IEEE Transactions on Geoscience and Remote Sensing*, 52 (2):1142–1156, FEB 2014. doi: 10.1109/TGRS.2013.2247768.

S. Casadio and O. Arino. Monitoring the south atlantic anomaly using atsr instrument series. *Advances in Space Research*, 48(6):1056–1066, SEP 15 2011. doi: 10.1016/j.asr.2011.05.014.

T. A. Croft. Burning waste gas in oil fields. *Nature*, 245(5425):375–376, OCT 1973. doi: 10.1038/245375a0.

T. A. Croft. Nighttime images of the earth from space. *Scientific American*, 239:86–98, 1978. doi: 10.1038/scientificamerican0778-86.

I. Csiszar, W. Schroeder, L. Giglio, E. Ellicott, K. P. Vadrevu, C. O. Justice, and B. Wind. Active fires from the suomi npp visible infrared imaging radiometer suite: Product status and first evaluation results. *Journal of Geophysical Research: Atmospheres*, 119(2):85–96, 2013.

D. K. Davies, S. Ilavajhala, M. M. Wong, and C. O. Justice. Fire information for resource management system: Archiving and distributing modis active fire data. *IEEE Transactions on Geoscience and Remote Sensing*, 47(1):72–79, JAN 2009. doi: 10.1109/TGRS.2008.2002076.

L. G. Dickinson, E. B. III, and W. S. Burgmann. *Defense Meteorological Satellite Program (DMSP) User's Guide*. Air Weather Service, U.S. Air Force, DEC 1974.

J. Dozier. A method for satellite identification of surface-temperature fields of subpixel resolution. *Remote Sensing of Environment*, 11(3):221–229, 1981. doi: 10.1016/0034-4257(81)90021-3.

O. Dubovik, B. N. Holben, Y. J. Kaufman, M. Yamasoe, A. Smirnov, D. Tanre, and I. Slutsker. Single-scattering albedo of smoke retrieved from the sky radiance and so-

lar transmittance measured from ground. *Journal of Geophysical Research-Atmospheres*, 103(D24):31903–31923, DEC 27 1998. doi: 10.1029/98JD02276.

T. J. Duck, B. J. Firanski, D. B. Millet, A. H. Goldstein, J. Allan, R. Holzinger, D. R. Worsnop, A. B. White, A. Stohl, C. S. Dickinson, and A. van Donkelaar. Transport of forest fire emissions from alaska and the yukon territory to nova scotia during summer 2004. *Journal of Geophysical Research-Atmospheres*, 112(D10):D10S44, MAY 19 2007. doi: 10.1029/2006JD007716.

C. Elvidge, K. Baugh, E. Kihn, H. Kroehl, and E. Davis. Mapping city lights with nighttime data from the dmsp operational linescan system. *Photogrammetric Engineering and Remote Sensing*, 63(6):727–734, JUN 1997. PT: J; NR: 10; TC: 244; J9: PHOTOGRAMM ENG REM S; PG: 8; GA: XC407; UT: WOS:A1997XC40700009.

C. Elvidge, K. Baugh, J. Dietz, T. Bland, P. Sutton, and H. Kroehl. Radiance calibration of dmsp-ols low-light imaging data of human settlements. *Remote Sensing of Environment*, 68(1):77–88, APR 1999. doi: 10.1016/S0034-4257(98)00098-4.

C. D. Elvidge, M. Zhizhin, F.-C. Hsu, and K. E. Baugh. Viirs nightfire: Satellite pyrometry at night. *Remote Sensing*, 5(9):4423–4449, SEP 2013. doi: 10.3390/rs5094423.

M. Flannigan and T. Vonderhaar. Forest-fire monitoring using noaa satellite avhrr. *Canadian Journal of Forest Research-Revue Canadienne De Recherche Forestiere*, 16(5):975–982, OCT 1986. doi: 10.1139/x86-171.

S. Flasse and P. Ceccato. A contextual algorithm for avhrr fire detection. *International Journal of Remote Sensing*, 17(2):419–424, JAN 20 1996.

S. P. Flasse, S. N. Trigg, P. N. Ceccato, A. H. Perryman, A. T. Hudak, M. W. Thompson, B. H. Brockett, M. Drame, T. Ntabeni, P. E. Frost, T. Landmann, and J. L. le Roux.

Warming and earlier spring increase western US forest wildfire activity. 2004. ISBN 1-919833-65-X.

L. Giglio and J. D. Kendall. Evaluation of global fire detection algorithms using simulated avhrr infrared data. *International Journal of Remote Sensing*, 20(10):1947–1985, JUL 10 1999. doi: 10.1080/014311699212290.

L. Giglio and J. D. Kendall. Application of the dozier retrieval to wildfire characterization - a sensitivity analysis. *Remote Sensing of Environment*, 77(1):34–49, JUL 2001. doi: 10.1016/S0034-4257(01)00192-4.

L. Giglio, J. Descloitres, C. O. Justice, and Y. J. Kaufman. An enhanced contextual fire detection algorithm for modis. *Remote Sensing of Environment*, 87(2-3):273–282, OCT 15 2003. doi: 10.1016/S0034-4257(03)00184-6.

W. M. Hao, D. E. Ward, G. Olbu, and S. P. Baker. Emissions of co2, co, and hydrocarbons from fires in diverse african savanna ecosystems. *Journal of Geophysical Research-Atmospheres*, 101(D19):23577–23584, OCT 30 1996. doi: 10.1029/95JD02198.

D. A. Hastings and W. J. Emery. The advanced very high-resolution radiometer (avhrr) - a brief reference guide. *Photogrammetric Engineering and Remote Sensing*, 58(8):1183–1188, AUG 1992. PT: J; TC: 20; UT: WOS:A1992JF23200045.

K. Haynes, J. Handmer, J. McAneney, A. Tibbits, and L. Coates. Australian bushfire fatalities 1900-2008: exploring trends in relation to the "prepare, stay and defend or leave early" policy. *Environmental Science & Policy*, 13(3):185–194, MAY 2010. 10.1016/j.envsci.2010.03.002.

D. Hillger, T. Kopp, T. Lee, D. Lindsey, C. Seaman, S. Miller, J. Solbrig, S. Kidder, S. Bachmeier, T. Jasmin, and T. Rink. First-light imagery from suomi npp viirs. *Bulletin of the*

American Meteorological Society, 94(7):1019–1029, JUL 2013. doi: 10.1175/BAMS-D-12-00097.1.

P. J. Huber. 1972 wald lecture - robust statistics - review. *Annals of Mathematical Statistics*, 43(4):1041–, 1972. doi: 10.1214/aoms/1177692459.

C. Ichoku and Y. J. Kaufman. A method to derive smoke emission rates from modis fire radiative energy measurements. *IEEE Transactions on Geoscience and Remote Sensing*, 43(11):2636–2649, NOV 2005. doi: 10.1109/TGRS.2005.857328.

C. Ichoku, L. Giglio, M. J. Wooster, and L. A. Remer. Global characterization of biomass-burning patterns using satellite measurements of fire radiative energy. *Remote Sensing of Environment*, 112(6):2950–2962, JUN 16 2008. doi: 10.1016/j.rse.2008.02.009.

O. S. Ismail and G. E. Umukoro. Global impact of gas flaring. *Energy and Power Engineering*, Vol. 4 No. 4:290–302, NOV 2012. doi: 10.4236/epe.2012.44039.

JPSS. *Joint Polar Satellite System (JPSS) VIIRS active fires: Fire mask Algorithm Theoretical Basis Document (ATDB)*, APR 2011a. 474-00030, released April 22, 2011, available at http://npp.gsfc.nasa.gov/documents.html.

JPSS. *Joint Polar Satellite System (JPSS) VIIRS Geolocation Algorithm Theoretical Basis Document (ATBD)*, JUL 2011b. 474-00053, released July 31, 2011, available at http://npp.gsfc.nasa.gov/documents.html.

C. Justice, L. Giglio, S. Korontzi, J. Owens, J. Morisette, D. Roy, J. Descloitres, S. Alleaume, F. Petitcolin, and Y. Kaufman. The modis fire products. *Remote Sensing of Environment*, 83(1-2):244–262, NOV 2002. doi: 10.1016/S0034-4257(02)00076-7.

C. O. Justice, J. D. Kendall, P. R. Dowty, and R. J. Scholes. Satellite remote sensing of fires during the safari campaign using noaa advanced very high resolution radiometer. *Journal*

of Geophysical Research-Atmospheres, 101(D19):23851–23863, OCT 30 1996 1996. doi: 10.1029/95JD00623.

Y. J. Kaufman, D. Tanre, H. R. Gordon, T. Nakajima, J. Lenoble, R. Frouin, H. Grassl, B. M. Herman, M. D. King, and P. M. Teillet. Passive remote sensing of tropospheric aerosol and atmospheric correction for the aerosol effect. *Journal of Geophysical Research-Atmospheres*, 102(D14):16815–16830, JUL 27 1997. doi: 10.1029/97JD01496.

Y. J. Kaufman, C. O. Justice, L. P. Flynn, J. D. Kendall, E. M. Prins, L. Giglio, D. E. Ward, W. P. Menzel, and A. W. Setzer. Potential global fire monitoring from eos-modis. *Journal of Geophysical Research-Atmospheres*, 103(D24):32215–32238, DEC 27 1998a. doi: 10.1029/98JD01644.

Y. J. Kaufman, R. G. Kleidman, and M. D. King. Scar-b fires in the tropics: Properties and remote sensing from eos-modis. *Journal of Geophysical Research-Atmospheres*, 103(D24): 31955–31968, DEC 27 1998b. doi: 10.1029/98JD02460.

Y. J. Kaufman, D. Tanre, and O. Boucher. A satellite view of aerosols in the climate system. *Nature*, 419(6903):215–223, SEP 12 2002. doi: 10.1038/nature01091.

J. Lagarias, J. Reeds, M. Wright, and P. Wright. Convergence properties of the nelder-mead simplex method in low dimensions. *Siam Journal on Optimization*, 9(1):112–147, DEC 21 1998. doi: 10.1002/2013JD020453.

T. E. Lee, S. D. Miller, F. J. Turk, C. Schueler, R. Julian, S. Deyo, P. Dills, and S. Wang. The npoess viirs day/night visible sensor. *Bulletin of the American Meteorological Society*, 87(2):191–199, 02 2006. URL http://0-search.ebscohost.com.library.unl.edu/login.aspx?direct=true&db=aph&AN=19897069&site=ehost-live. doi: 10.1175/BAMS-87-2-191.

Z. Li, Y. J. Kaufman, C. Ichoku, R. Fraser, A. Trischenko, L. Giglio, J.-Z. Jin, and X. Yu. *A review of avhrr-based active fire detection algorithms: Principles, limitations, and recommendations*. SPB Academic Publishing bv a , P. O. Box 97747, 2509 GC, The Hague, Netherlands, P. O. Box 97747, 2509 GC, The Hague, Netherlands, 2001. ISBN 90-5103-140-8 (paper). PT: B; UT: BCI:BCI200200156136 ME: print; NR: 0; TC: 22.

L. B. Liao, S. Weiss, S. Mills, and B. Hauss. Suomi npp viirs day-night band on-orbit performance. *Journal of Geophysical Research-Atmospheres*, 118(22):12705–12718, NOV 27 2013. doi: 10.1002/2013JD020475.

J. M. Lobert and J. Warnatz. *Emissions from the combustion process in vegetation*, volume 13. 1993 1993.

M. Matson and J. Dozier. Identification of subresolution high-temperature sources using a thermal ir sensor. *Photogrammetric Engineering and Remote Sensing*, 47(9):1311–1318, SEP 1981.

M. Matson and B. Holben. Satellite detection of tropical burning in brazil. *International Journal of Remote Sensing*, 8(3):509–516, MAR 1987.

S. Miller, S. Haddock, C. Elvidge, and T. Lee. Detection of a bioluminescent milky sea from space. *Proceedings of the National Academy of Sciences of the United States of America*, 102(40):14181–14184, OCT 4 2005. doi: 10.1073/pnas.0507253102.

S. D. Miller, S. P. Mills, C. D. Elvidge, D. T. Lindsey, T. F. Lee, and J. D. Hawkins. Suomi satellite brings to light a unique frontier of nighttime environmental sensing capabilities. *Proceedings of the National Academy of Sciences of the United States of America*, 109(39): 15706–15711, 09/25 2012. doi: 10.1073/pnas.1207034109.

K. Muirhead and A. Cracknell. Identification of gas flares in the north-sea using satellite data. *International Journal of Remote Sensing*, 5(1):199–212, 1984.

newsru.com. Khanty-mansi autonomous district extracted 10 billion tons of oil, 2012. URL: http://www.newsru.com/finance/22feb2012/ugra.html.

The Ministry of Environment of the Federal Republic of Nigeria. Nigeria's first national communication under the united nations framework convention on climate change, 2003.

D. Peterson and J. Wang. A sub-pixel-based calculation of fire radiative power from modis observations: 2. sensitivity analysis and potential fire weather application. *Remote Sensing of Environment*, 129:231–249, FEB 15 2013. doi: 10.1016/j.rse.2012.10.020.

D. Peterson, J. Wang, C. Ichoku, E. Hyer, and V. Ambrosia. A sub-pixel-based calculation of fire radiative power from modis observations: 1 algorithm development and initial assessment. *Remote Sensing of Environment*, 129:262–279, FEB 15 2013. doi: 10.1016/j.rse.2012.10.036.

D. A. Peterson, E. J. Hyer, J. R. Campbell, M. D. Fromm, J. W. Hair, C. F. Butler, and M. A. Fenn. The 2013 rim fire: Implications for predicting extreme fire spread, pyroconvection, and smoke emissions. *Bulletin of the American Meteorological Society*, 2014. doi: 10.1175/BAMS-D-14-00060.1.

T. N. Polivka, E. J. Hyer, J. Wang, and D. A. Peterson. First global analysis of saturation artifacts in the viirs infrared channels and the effects of sample aggregation. *Ieee Geoscience and Remote Sensing Letters*, 12(6):1262–1266, JUN 2015.

E. Prins and W. Menzel. Geostationary satellite detection of biomass burning in south-america. *International Journal of Remote Sensing*, 13(15):2783–2799, OCT 1992.

PT: J; NR: 38; TC: 144; J9: INT J REMOTE SENS; PG: 17; GA: JT898; UT: WOS:A1992JT89800004.

E. Prins and W. Menzel. Trends in south-american biomass burning detected with the goes visible infrared spin scan radiometer atmospheric sounder from 1983 to 1991. *Journal of Geophysical Research-Atmospheres*, 99(D8):16719–16735, AUG 20 1994. PT: J; UT: WOS:A1994PC94400033.

E. Prins, J. Feltz, W. Menzel, and D. Ward. An overview of goes-8 diurnal fire and smoke results for scar-b and 1995 fire season in south america. *Journal of Geophysical Research-Atmospheres*, 103(D24):31821–31835, DEC 27 1998. PT: J; UT: WOS:000077967000023.

V. Ramanathan, P. J. Crutzen, J. Lelieveld, A. P. Mitra, D. Althausen, J. Anderson, M. O. Andreae, W. Cantrell, G. R. Cass, C. E. Chung, A. D. Clarke, J. A. Coakley, W. D. Collins, W. C. Conant, F. Dulac, J. Heintzenberg, A. J. Heymsfield, B. Holben, S. Howell, J. Hudson, A. Jayaraman, J. T. Kiehl, T. N. Krishnamurti, D. Lubin, G. McFarquhar, T. Novakov, J. A. Ogren, I. A. Podgorny, K. Prather, K. Priestley, J. M. Prospero, P. K. Quinn, K. Rajeev, P. Rasch, S. Rupert, R. Sadourny, S. K. Satheesh, G. E. Shaw, P. Sheridan, and F. P. J. Valero. Indian ocean experiment: An integrated analysis of the climate forcing and effects of the great indo-asian haze. *Journal of Geophysical Research-Atmospheres*, 106(D22):28371–28398, NOV 27 2001. doi: 10.1029/2001JD900133.

J. S. Reid, E. J. Hyer, E. M. Prins, D. L. Westphal, J. Zhang, J. Wang, S. A. Christopher, C. A. Curtis, C. C. Schmidt, D. P. Eleuterio, K. A. Richardson, and J. P. Hoffman. Global monitoring and forecasting of biomass-burning smoke: Description of and lessons from the fire locating and modeling of burning emissions (flambe) program. *Ieee Journal of Selected Topics in Applied Earth Observations and Remote Sensing*, 2(3):144–162, SEP 2009. doi: 10.1109/JSTARS.2009.2027443.

J. Robinson. Fire from space - global fire evaluation using infrared remote-sensing. *International Journal of Remote Sensing*, 12(1):3–24, JAN 1991.

W. Schroeder, P. Oliva, L. Giglio, and I. A. Csiszar. The new viirs 375m active fire detection data product: Algorithm description and initial assessment. *Remote Sensing of Environment*, 143:85–96, MAR 5 2014. doi: 10.1016/j.rse.2013.12.008.

G. R. van der Werf, J. T. Randerson, L. Giglio, G. J. Collatz, M. Mu, P. S. Kasibhatla, D. C. Morton, R. S. DeFries, Y. Jin, and T. T. van Leeuwen. Global fire emissions and the contribution of deforestation, savanna, forest, agricultural, and peat fires (1997-2009). *Atmospheric Chemistry and Physics*, 10(23):11707–11735, 2010. doi: 10.5194/acp-10-11707-2010.

J. Wang, S. A. Christopher, U. S. Nair, J. S. Reid, E. M. Prins, J. Szykman, and J. L. Hand. Mesoscale modeling of central american smoke transport to the united states: 1. "top-down" assessment of emission strength and diurnal variation impacts. *Journal of Geophysical Research-Atmospheres*, 111(D5):D05S17, MAR 9 2006. doi: 10.1029/2005JD006416.

R. Welch. Monitoring urban-population and energy-utilization patterns from satellite data. *Remote Sensing of Environment*, 9(1):1–9, 1980. doi: 10.1016/0034-4257(80)90043-7.

A. L. Westerling, H. G. Hidalgo, D. R. Cayan, and T. W. Swetnam. Warming and earlier spring increase western us forest wildfire activity. *Science*, 313(5789):940–943, AUG 18 2006. doi: 10.1126/science.1128834.

R. E. Wolfe, G. Lin, M. Nishihama, K. P. Tewari, J. C. Tilton, and A. R. Isaacman. Suomi npp viirs prelaunch and on-orbit geometric calibration and characterization. *Journal of Geophysical Research-Atmospheres*, 118(20), OCT 27 2013. doi: 10.1002/jgrd.50873.

World Bank. Estimated flared volumes from satellite data, 2007-2011, 2014. URL: http://go.worldbank.org/D03ET1BVD0.